Comparing Infrared Cloud Detection Algorithms to Improve the Current National Weather Prediction Infrared Cloud Detection Algorithm

Brianne R Andersen

A Thesis submitted in partial fulfillment of

the requirements for the degree of

Master of Science

(Atmospheric and Oceanic Sciences)

at the

UNIVERSITY OF WISCONSIN-MADISON

May 2022

Candidate for the degree of MS
Fall 2021-2022

Andersen,Brianne

9081852379

Major: *Atmospheric and Oceanic Sciences MS - Research Program*

The undersigned report that all degree requirements have been met on *Wednesday, November 10, 2021*.

We recommend that the above named candidate be awarded the degree indicated.

Committee Member Name		Committee Member Signature	Date	
L'Ecuyer,Tristan S	Advisor	*Tristan L'Ecuyer*	*1/14/2022 10:31:22 PM*	
MENZEL, WOLFGANG P		*W Paul Menzel*	*1/18/2022 9:36:42 AM*	Reader
PETTY, GRANT W		*Grant W Petty*	*1/19/2022 9:03:46 AM*	Reader

☑ Student may continue for a PHD in the same program

☐ Student is required to deposit a thesis in Memorial Library

Abstract

Comparing Infrared Cloud Detection Algorithms to Improve the Current National Weather Prediction Infrared Cloud Detection Algorithm

by Brianne R Andersen

The current National Center for Environmental Prediction (NCEP) high resolution infrared (IR) cloud detection algorithm was originally designed for the High-resolution IR Sounder (HIRS). HIRS has since been outdated by the Cross-track IR Sounder (CrIS), which has significantly higher spectral resolution and smaller channel bandwidth. However, the current algorithm has yet to fully modernize, and does not utilize the full capabilities CrIS offers. The purpose of this project was to bring the NCEP's algorithm into the modern age by comparing the NCEP algorithm with CO_2 Slicing, Dual Regression (DR), and European Centre for Medium-Range Weather Forecasts Cloud and Aerosol Detection Algorithm (ECMWF), all of which take advantage of CrIS and its high spectral resolution potential. After a thorough investigation, CO_2 Slicing was considered the principal algorithm to improve NCEP.

Spatial points where CO_2 Slicing differed from NCEP were examined to determine which algorithm was valid, utilizing collocated Visible Infrared Imaging Radiometer Suite (VIIRS) as observed data/truth, comparison plots, and statistical analysis. Suggested implementable changes to the current were proposed from the analysis of spatial points where

NCEP incorrectly classified the point but CO2 Slicing correctly classified the point. Additionally, suggestions of CrIS channels to add to NCEP clear sky scheme were proposed to help in removing cloud contaminations.

Acknowledgements

This project truly took a village to accomplish, and there are so many people to thank.

A huge thank you to my research team, including Jim Jung (PI/CIMSS/NOAA), Paul Menzel (CIMSS), and Sharon Nebuda (CIMSS). Each of them guided me through the process of research, becoming a scientist, and provided an environment where I could feel comfortable to ask many questions.

There were so many collaborators to thank as well, including Andrew Collard (NCEP/EMC), Andrew Heidinger (NESDIS/ASPB), Daryl Kleist (NCEP), Emily Liu (NCEP), Haixia Liu (NCEP), and William McCarty (NASA/GMAO).

Funding was graciously provided from the JPSS Program Office by Mitch Goldberg, Satya Kalluri, and Lihang Zhao.

I must also thank Tristan L'Ecuyer. As my academic advisor, he helped me greatly navigate through graduate school, advising me on courses to take, and provided a support network in the form of his research group.

In addition to the L'Ecuyer research group, my entire graduate cohort provided much need emotional and personal support throughout the past few years.

Outside of AOSS, I have a great community of undergraduate friends, Jewish community members, and pervious educators that I owe such gratitude towards. A special thank you to Grant Petty, who in addition to being one of my graduate professors, served on my masters committee.

And perhaps the most important support came from my family. I will never be able to truly thank my mom, Sharon, my dad, Kris, and my sisters, Jordan and Ellery, for helping me get to this point. I appreciate you all so much.

Contents

List of Figures

Abbreviations

BT	brightness temperature
CO2 Slicing	CO2 Slicing technique
CrIS	Cross Track IR Sounder
CRTM	Community Radiative Transfer Model
CSPP	Community Satellite Processing Package
CTP	cloud top pressure
DR	Dual Regression
ECMWF	European Centre for Medium-Range Weather Forecasts
ECMWF-CAD	ECMWF Cloud and Aerosol Detection Algorithm
ε	emissivity
FV3GFS	Finite-Volume Cubed-Sphere Global Forecast System
FOV	field of view
HIRS	High-resolution Infrared Sounder
HSRTV	HyperSpectral ReTrieVal
IR	infrared
JPSS	Joint Polar Satellite System
NASA	National Aeronautics and Space Administration
NCEP	National Center for Environmental Prediction
NCEP Algorithm	NCEP cloud detection algorithm clear sky scheme
NOAA	National Oceanic and Atmospheric Administration
NWP	National Weather Prediction
PBL	planetary boundary layers top height
PCRTM	Principal Component-based Radiative Transfer Model
SSEC	Space Science and Engineering Center
Trop	tropopause height
UW-Madison	University of Wisconsin-Madison

Research Objective

The objective of the research described in this paper is to improve the current National Center for Environmental Prediction (NCEP) infrared (IR) cloud detection algorithm (henceforth called NCEP Algorithm). By way of better detecting clouds, this research also serves to improve the clear sky detection. This paper proposes techniques which could offer improvements to the NCEP Algorithm by

I. identifying and removing cloud contaminated points, and

II. increasing the number of clear sky points to be assimilated.

The objectives correctly imply that the NCEP Algorithm may be significantly misclassifying measurements as cloudy or clear. This results in incorrect or unnecessary bias corrections, poorly executed assimilations, and smaller datasets used in the assimilation system. One application of the NCEP Algorithm is providing cloud information (e.g., cloud top pressure (CTP) and cloud effective emissivity (Nε)). Accurate CTP and Nε calculations are vital information for modeling temperature and humidity atmospheric profiles (Lim et al., 1989, Wang et al., 2017). This, in turn, is used to forecast weather systems on multiple meteorological scales, such as mesoscale for precipitation systems

or synoptic scale for hurricanes. This lends credence to the importance of an accurate NCEP Algorithm.

For an optimized clear sky assimilation, the input would only accept high-spectral resolution IR radiances from field of view (FOV) measurements that have not been affected by clouds. The more FOVs incorporated into the algorithm, the more accurate the assimilation and bias correction would be. With an improved algorithm, cloudy FOVs would be rejected and more clear FOVs would be identified and assimilated. As will be described in the NCEP Algorithm Explained section of this paper, the NCEP Algorithm is relatively conservative in the classification of clear sky. This results in relatively few FOVs classified as clear, potentially losing valuable data for downline processing. Even with this conservative approach, some cloudy FOVs are still misclassified as clear, which produces a cold bias in the assimilation. This is especially true for FOVs with high level (above 200 hPa) optically thin cirrus clouds.

For this study, three algorithms were compared with the NCEP Algorithm to investigate if they better classify measurements within a FOV as cloudy or clear, and to note the CTP and Nε values:

i. Dual Regression (DR) described by Smith et al. (2012)

ii. European Centre for Medium-Range Weather Forecasts Cloud and Aerosol Detection Algorithm (henceforth called ECMWF-CAD) described by McNally and Watts (2003)

iii. CO2 Slicing described by Wylie and Menzel (1989).

The focus of this work is on data from the Cross-track Infrared Sounder (CrIS). Each algorithm is currently being used in operations in some capacity, most directly demonstrated with ECMWF-CAD at the European Centre. This paper outlines the process used to compare each of the algorithms against the NCEP Algorithm and suggests the best preforming algorithm. A description of the 4 algorithms and the data used is followed by an account of the methodology for algorithm performance analysis, noting the variability taken into account, assumptions made, and plots used. The algorithms are evaluated for performance initially over ocean only (limiting the data set to a relatively uniform earth surface) and then globally (including complex land surfaces) for one day in January, April, July, and October covering the four seasons. A summary of the results and recommendations for consideration by NCEP is offered in the discussion and conclusion.

Methodology

2.1 Data Used

For all algorithms investigated in this paper, observation brightness temperature (BT) and transmittance data was required as an input, specifically coming from CrIS. CO2 Slicing, ECMWF-CAD, and the NCEP Algorithm further required simulated clear BT from a model as an input. The model data, in this case, came from the analyses data, which will be further discussed below. For this project, Visual Infrared Imaging Radiometer Suite (VIIRS) data were used as visual confirmation of algorithm outputs, and were assumed to be observation truth in most cases. This section provides a brief description of the data used.

2.1.1 CrIS

CrIS is a sounding instrument part of the Joint Polar Satellite System (JPSS)—a NOAA and NASA program—currently aboard Suomi-NPP (launched 2011-28-10) and NOAA-20 (launched 2017-18-11). It is the successor to High-resolution IR Radiation Sounder (HIRS). Note, only CrIS data from NOAA-20 was used in this paper. It hosts 2211 spectral channels, ranging from 650 cm^{-1} to 2250 cm^{-1} (Iturbide, 2021)), of which the NCEP Algorithm uses a subset of 431 channels. Although all 2211 channels were input into DR

and the subset were input into the NCEP Algorithm and ECMWF-CAD, channels with smaller wavenumbers were exclusively used in CO2 Slicing, and were primarily used in analysis, as larger wavenumbers tend to be associated with surface features. Frequency bands in the longwave/small wavenumber have spectral resolution of 0.625 cm^{-1}. The spatial resolution of a CrIS FOV is 13.5 km at nadir. The temporal resolution varies by latitude, with a full orbit scan taking 101 minutes, resulting in twice daily passes over equatorial regions and up to 14 daily passes at the poles. Ignoring orbital track features, CrIS completes a nearly full global scan in approximately 12 hours.

2.1.2 VIIRS

VIIRS, like CrIS, is a part of JPSS and is on SNPP and NOAA-20. The standard spatial resolution at nadir is 750 m, and can be colocated with CrIS at 13.5 km. For the purposes of this project as visual confirmation, 24-hour simulated true color composites were used. True color was simulated via channels 5, 4, and 3, or 0.672 μm, 0.555 μm, and 0.488 μm respectively (NASA, 2021). Note, as this is visible data, the imagery is limited to daylight hours defined as FOVs with local solar zenith angle $\geq 84°$. Additionally, colocated VIIRS CTP and Nε approximations were considered as an additional estimate of CTP and Nε.

2.1.3 Analyses

Model calculated clear sky BTs were an input to the NCEP Algorithm, CO2 Slicing, and ECMWF-CAD. These values came by way of the Community Radiative Transfer Model (CRTM). The CRTM was developed via a conglomeration of multiple radiative transfer

models (RTM). A RTM is a way to model the radiative processes between incoming solar
as well as outgoing earth radiation and the atmosphere, and the earth's surface. Every
RTM uses assumptions to approximate the radiative system, but each essentially boils
down to a summation of incoming shortwave solar radiation, and longwave and shortwave
absorbed, reflected, and refracted radiation. For this project, the model data came from
Finite-Volume Cubed-Sphere Global Forecast System (FV3GFS). FV3GFS is a part of
the NCEP Central Operations (NCO) weather forecast suite, and outputs values such as
ambient atmospheric temperature and pressure profiles, water vapor content, etc. (Lin
et al., 2017). These variables are then analyzed via the Gridpoint Statistical Interpolation
(GSI) software in time and space. Next, the FV3GFS GSI analyses data are inputted
into the CRTM. The outputs of interest from the CRTM for the algorithms are simulated
clear sky radiance, transmittance, and weighting values at multiple pressure levels (128
in the case of analyses) at every CrIS wavenumber (JCSDA, 2021). From here on, the
term "analyses", abbreviated as A, will refer to the channel equivalent clear radiances
from the CRTM via the FV3GFS atmospheric analyses.

2.2   Explanation of the NCEP Algorithm

The current NCEP Algorithm, as outlined in Eyre and Menzel (1989), works via compar-
ing clear analyses calculated radiances to observed IR radiances at each model layer using
the channel's/wavenumber's Jacobian at the specific model layer. For each IR profile, the
NCEP Algorithm will output a binary cloud mask value of cloudy or clear. If cloudy,
the NCEP algorithm will determine the model layer where the cloud resides and estimate

its cloud optical thickness (COT). With this information, the NCEP algorithm will then determine which channels/wavenumbers are contaminated by clouds.

The NCEP Algorithm assumes:

- Clouds are single layered. Therefore, for each cloudy FOV, there is only one CTP and one COT value.

- The cloud BT is the same as the environmental/surrounding pressure level calculated BT.

- Integration of radiance values are taken from the top of the atmosphere to the surface in clear FOVs, or to the CTP in cloudy FOVs. However, clouds are searched from the surface to the tropopause (Trop).

- The observed BT from a CTP to the surface are similar in value due to the nature of satellite retrievals.

- All clouds are taken to be opaque, therefore, effective emissivity is assumed to be equal to 1.

- Smaller IR wavenumbers are more sensitive to features higher up in the atmosphere.

The following is the algorithmic protocol of the NCEP Algorithm. A visual representation, is provided as Figure 2.1.

Quality Control Selected Channels

Analysis Model BT

$$BT_A(FOV) = \begin{bmatrix} BT_A(\nu_1, P_m) & \cdots & BT_A(\nu_n, P_m) \\ \vdots & \ddots & \vdots \\ BT_A(\nu_1, P_1) & \cdots & BT_A(\nu_n, P_1) \end{bmatrix}$$

Observed BT

$$BT_O(FOV) = \begin{bmatrix} BT_O(\nu_1) \\ \vdots \\ BT_O(\nu_n) \end{bmatrix}$$

Calculate Weighted Difference Between Pressure Levels

$$\delta(\nu_a, P_{b,b-1}) = \big(BT_A(\nu_a, P_b) - BT_A(\nu_a, P_{b-1})\big) * W(\nu_a, P_{b,b-1})$$

$$\delta(FOV) = \begin{bmatrix} \delta(\nu_1, P_{m,m-1}) & \cdots & \delta(\nu_n, P_{m,m-1}) \\ \vdots & \ddots & \vdots \\ \delta(\nu_1, P_{2,1}) & \cdots & \delta(\nu_n, P_{2,1}) \end{bmatrix}$$

Calculate Cloud Percent Between Pressure Layer

$$CLD_\%(P_{b,b-1}) = \frac{\sum_{i=1}^n BT_O(\nu_i, P_{b,b-1})\delta(\nu_i, P_{b,b-1})}{\sum_{i=1}^n \big(\delta(\nu_i, P_{b,b-1})\big)^2}, \qquad 0 \le CLD_\%(P_{b,b-1}) \le 1$$

$$CLD_\%(FOV) = \begin{bmatrix} CLD_\%(P_{m,m-1}) \\ \vdots \\ CLD_\%(P_{2,1}) \end{bmatrix}$$

Calculate Sum of Observed minus Weighted Model BT Between Pressure Levels

$$sum(P_{b,b-1}) = \sum_{i=1}^n \big(BT_O(\nu_i, P_{b,b-1}) - CLD_\%(P_{b,b-1}) * \delta(\nu_i, P_{b,b-1})\big)^2$$

$$sum(FOV) = \begin{bmatrix} sum(P_{m,m-1}) \\ \vdots \\ sum(P_{2,1}) \end{bmatrix}$$

Search for CTP (with surface fog and cloud test)

$$CTP(FOV) = \begin{cases} P_{2,1} & 0.75 > sum_3(P_{2,1}) \ne 0 \\ P_{b,b-1} & 1^{st}\ occurance\ sum_3(P_{b-1,b-2}) > sum_3(P_{b,b-1}) \ne 0 \\ Clear & all\ else \end{cases}$$
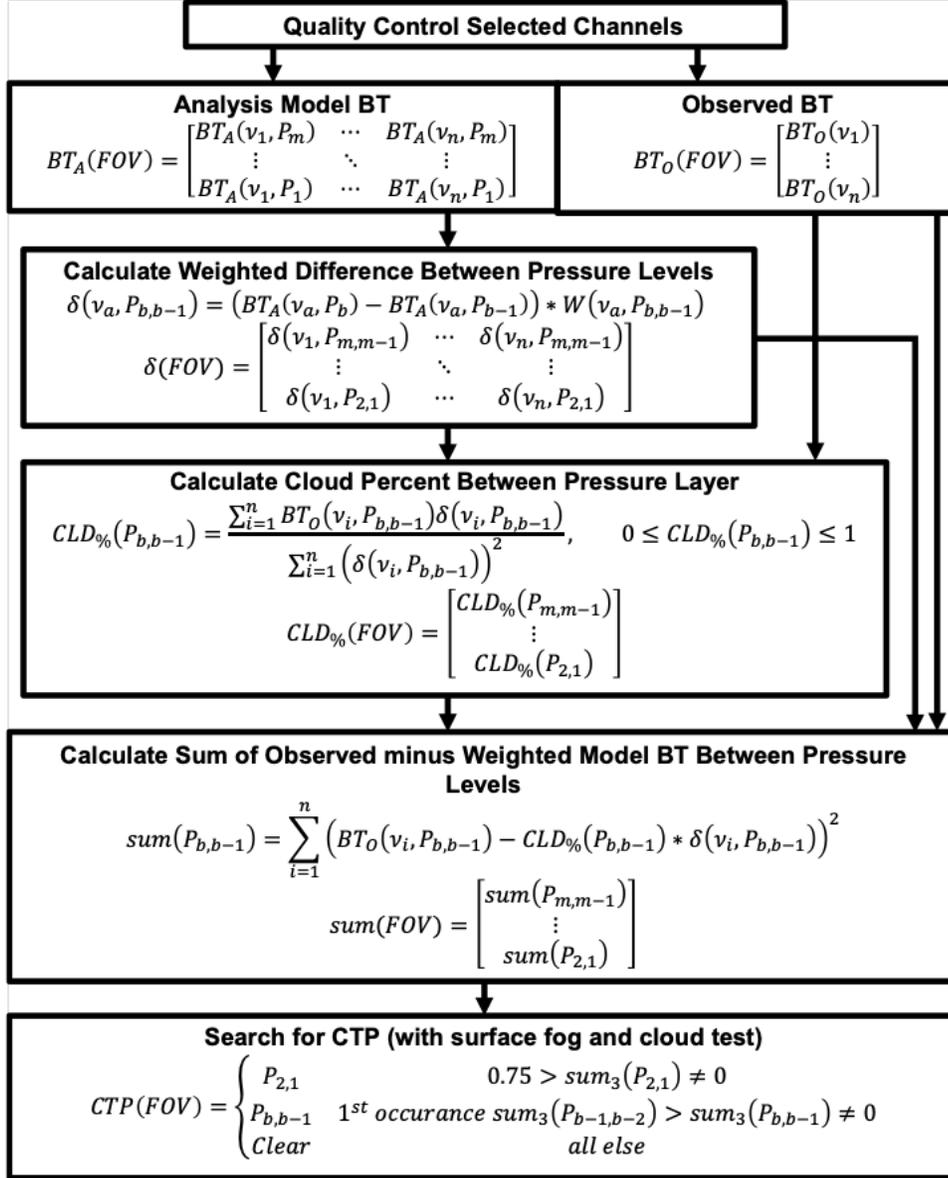
FIGURE 2.1: The NCEP Algorithm inputs clear BT from the analysis (A) model and observation (O) data from CrIS. The output clear or cloudy classification for each FOV is determined via this process. The end result is either a clear FOV where all wavenumbers are taken as clear, or a cloudy FOV a CTP value. For cloudy FOVs a separate method is used to determine clear and cloudy wavenumber.

1. A matrix of analyses clear BT is compiled for each FOV at every CrIS wavenumber. A second matrix of observed layer temperature difference for the same FOV is built and used later in the process. Pressure layers are assigned within the data file array values 1 to 127, where 1 is the near surface layer pressure and 127 is the top of the atmospheric profile. Note: layers above the tropopause are ignored.

$$FOV_{analyses} = \begin{bmatrix} BT_A(\nu_1, P_m) & \cdots & BT_A(\nu_n, P_m) \\ \vdots & \ddots & \vdots \\ BT_A(\nu_1, P_1) & \cdots & BT_A(\nu_n, P_1) \end{bmatrix}$$

$$FOV_O = \begin{bmatrix} BT_O(\nu_1) & \cdots & BT_O(\nu_n) \end{bmatrix}$$

2. A quality control algorithm is run to thin out the CrIS channels, eliminating contaminated (dust, smoke, etc.) and especially noisy channels.

3. A pressure layer is defined as the space between two sequential pressure levels. At each pressure layer where a CrIS channel is accepted by the quality control, the (analyses - observed) channel BT and pressure related weighted difference (Jacobian) of clear analyses BT is calculated, formulating an analyses weighted difference matrix.

$$\delta(\nu_a, P_{b,b-1}) = (BT_A(\nu_a, P_b) - BT_O(\nu_a, P_{b-1})) * W(\nu_a, P_{b,b-1})$$

$$FOV_\delta = \begin{bmatrix} \delta(\nu_1, P_{m,m-1}) & \cdots & \delta(\nu_n, P_{m,m-1}) \\ \vdots & \ddots & \vdots \\ \delta(\nu_1, P_{2,1}) & \cdots & \delta(\nu_n, P_{2,1}) \end{bmatrix}$$

4. This weighted difference value is then summed through all channels/wavenumbers at each pressure layer in two ways. The first multiplies this value at each wavenumber to the corresponding (analyses - observed) BT, again taking the sum of all wavenumbers at each pressure level.

$$sum_1(P_{b,b-1}) = \sum_{i=1}^{n} \Delta BT(\nu_i)\delta(\nu_i, P_{b,b-1})$$

$$FOV_{sum_{(1)}} = \begin{bmatrix} sum_1(P_{m,m-1}) \\ \vdots \\ sum_1(P_{2,1}) \end{bmatrix}$$

The second sum is effectively the sum of the squared weighted difference of analyses BT at each pressure layer.

$$sum_2(P_{b,b-1}) = \sum_{i=1}^{n} \left(\delta(\nu_i, P_{b,b-1})\right)^2$$

$$FOV_{sum_{(2)}} = \begin{bmatrix} sum_2(P_{m,m-1}) \\ \vdots \\ sum_2(P_{2,1}) \end{bmatrix}$$

5. The ratio of the two sum values from the previous step provides the cloud percentage at each pressure layer. If a pressure layer has an unrealistic value, that is a value not between 0% and 100%, then it is rejected as a realistic pressure layer.

$$CLD\%(P_{b,b-1}) = \frac{sum_1(P_{b,b-1})}{sum_2(P_{b,b-1})}$$

$$FOV_{CLD\%} = \begin{bmatrix} CLD\%(P_{m,m-1}), & 0 \le CLD\%(P_{m,m-1}) \le 1 \\ \vdots \\ CLD\%(P_{2,1}), & 0 \le CLD\%(P_{2,1}) \le 1 \end{bmatrix}$$

6. A final sum at each pressure layer (of (analyses - observation) BT cloud amount weighted analyses difference) is calculated. This one reduces the observed BT by using the weighted analyses difference and cloud percent values, then squares this difference. Another interpretation of this is the squared sum of weighted observed minus (analyses - observation) clear radiances through all considered wavenumbers at each pressure layer. This provides a value in which to compare pressure layers against one another to detect a cloud.

$$sum_3(P_{b,b-1}) = \sum_{i=1}^{n} [\Delta BT(\nu_i) - CLD\%(P_{b,b-1})\delta(\nu_i, P_{b,b-1})]^2$$

$$FOV_{sum_{(3)}} = \begin{bmatrix} sum_3(P_{m,m-1}) \\ \vdots \\ sum_3(P_{2,1}) \end{bmatrix}$$

7. The search for a cloud signal begins at the surface with a fog and surface cloud detection test. If sum_3 for a FOV at the first pressure layer, defined as $P_{2,1}$, is less than 0.75, then the NCEP Algorithm indicates fog or a surface level cloud. The CTP is then defined as halfway through pressure layer $P_{2,1}$.

$$sum_3(P_{2,1}) \leq 0.75 \rightarrow P_2 \leq CTP \leq P_1$$

However, if that statement is false, that is $sum_3(P_{2,1}) > 0.75$, then the NCEP Algorithm starts to compare pressure layer sum_3 values against one another. There is a caveat that sum_3 values should not be exactly 0, or that there must be differences between observed and analyses BT values.

$$FOV_{CTP} = \begin{bmatrix} sum_3(P_{m-1,m-2}) > sum_3(P_{m,m-1}) \to P_m \leq CTP \leq P_{m-1} \\ \vdots \\ sum_3(P_{x,x-1}) > sum_3(P_{x+1,x}) \to P_{x+1} \leq CTP \leq P_x \\ \vdots \\ sum_3(P_{2,1}) > sum_3(P_{3,2}) \to P_3 \leq CTP \leq P_2 \end{bmatrix}$$

A cloud is detected at the first pressure layer the upper layer is greater than the layer just below it. For example, a FOV has a cloud between pressure levels 40 and 41. At the surface level, the NCEP Algorithm will not detect surface fog or clouds. It will then compare layer 2, the layer comprised of the surface level and the first pressure level, sum_3 value to layer 3 sum_3 value (between pressure level 2 to level 3). In this instance, layer 2 will have a sum_3 value less than the layer 3 sum_3 value. For all layers in between the surface and the cloud, the sum_3 will be increasing with increasing height. However, at the cloud layer, the lower layer will have a higher sum_3 value than the upper layer. In the example, the sum_3 value for layer 40 (between pressure levels 39 and 40) will be more than the sum_3 value for layer 41 (between pressure levels 40 and 41). Therefore, the FOV will be classified as cloudy, and the CTP will be calculated as between pressure levels 40 and 41.

The NCEP Algorithm was developed during the era of and for the HIRS. HIRS, which was last launched on NOAA-19, has 19 IR channels. Its successor, CrIS, has significantly higher spectral resolution with 2211 IR channels. The NCEP Algorithm currently uses a subset of the available CrIS data, typically working with 431 of the 2211 channels.

However, not all 431 channels are used in every assimilation. For example, during a random assimilation, after a quality control is applied, only about 23% of the 431 channels were used (aka not monitored), and only 13.5% of the 431 channels were used in the clear sky scheme. That is, the NCEP Algorithm used 58 CrIS channels, nearly triple the number of HIRS channels, but a mere 2.6% of the 2211 CrIS channels.

Part of the investigation in this paper is to question this statistic, explicitly with the scope of the NCEP Algorithm. Is only using 2.6% of the available channels adequate in producing an accurate clear sky scheme? It is also important to question the quality of the selected channels, and how each channel is used. That is, are the selected CrIS channels utilizing CrIS' full potential as a sensor? Do they maximize the correct selection of clear sky FOVs, and if not would adding more channels and/or selecting different channels and/or assimilating the channels in a different way impact the accuracy of clear sky FOV detection? A noteworthy point, then, is that while the other algorithms have similar structures to the NCEP Algorithm, as will be demonstrated in the next section, possibly small assumption, process, and decision-making modifications could greatly affect the outcome.

2.3   The Alternate Algorithms Explained

2.3.1   Explanation of CO2 Slicing

CO2 Slicing, just as with the NCEP Algorithm, compares analyses and observed BT values throughout a FOV atmospheric profile to detect a cloud. CO2 Slicing also assumes

that clouds are single layered, clouds share similar observed BT and surrounding BT, and smaller IR wavenumbers are more sensitive to features higher up in the atmosphere. Additionally, it uses a top of atmosphere to surface approach in searching for a cloud, and a surface up approach in integration.

But CO2 Slicing has two basic structural differences that sets it apart from the NCEP Algorithm. First, CO2 Slicing only uses CO2 absorption channels, rather than the subset of 431 channels NCEP Algorithm uses (specifically spectrally close CO2 absorption paired). Moreover, only selected paired channels are used to detect clouds and CTP, relying on the aforementioned wavenumber and atmospheric height relationship. Secondly, CO2 Slicing does not rely on the assumption the NCEP Algorithm uses that clouds are opaque. Rather, if two wavenumbers are spectrally close to one another, then the ratio of their ε should be very similar.

$\varepsilon(\nu_1) \approx \varepsilon(\nu_2) \therefore \frac{\varepsilon(\nu_1)}{\varepsilon(\nu_2)} \approx 1$

This assumption allows for FOVs with optically thin clouds, specifically optically thin cirrus, to be classified as cloudy (Zhang and Menzel, 2002). These clouds are of particular interest as they are often non-detectable in the visible spectrum, and the NCEP Algorithm often misidentifies these FOVs as clear sky. Additionally, as explained by Sassen et al. (2002), sensors such as radar and lidar have proven effective at detecting thin clouds, but the lower spatial and temporal resolution of these sensors limits in their efficacy as secondary cloud detection measures.

The CO2 Slicing is encapsulated in this equation:

$$A_1(\nu) = R_A(\nu) - R_O(\nu)$$

$$A_2(\nu, P) = \int_{P_{PBL}}^{P} \tau(\nu, P) BT(\nu, T(P)) dP$$

$$N\varepsilon(\nu, P) = \frac{R_O(\nu) - R_A(\nu)}{BT(\nu, T(P))) - R_A(\nu)}$$

$$A_3(nu_1, \nu_2, P_{CLD}) = \frac{A_1(\nu_1)}{A_1(\nu_2)} - \left(\frac{N\varepsilon(\nu_1, P_{CLD})}{N\varepsilon(\nu_2, P_{CLD})}\right) \left(\frac{A_2(\nu_1, P_{CLD})}{A_2(\nu_2, P_{CLD})}\right)$$

$$CO_2(\nu_1, \nu_2) = P_{CLD} \rightarrow A_3(nu_1, \nu_2, P_{CLD}) \approx 0$$

(Note, the $N\varepsilon$ fraction on the right side of the equation was included for completion, but as perviously stated, is assumed to equal 1.)

Where:

ν = CrIS wavenumber

ν_1, ν_2 = paired, spectrally close CO2 absorption wavenumbers

P = pressure level

P_{SFC} = surface pressure

P_{CLD} = cloud pressure, as calculated by CO2 Slicing

$R_O(\nu)$ = observed radiance at some P and ν

$R_A(\nu)$ = analyses clear calculated radiance at some ν

$\tau(\nu, P)$ = analyses calculated transmittance at some ν

$BT(\nu, T(P)) = $ blackbody radiance from Planck's function, using temperature T at P

and ν

The original CO2 Slicing framework, as described in Wylie and Menzel (1989), was

adapted for this project to better employ the spectral resolution CrIS offers, including:

1. Defining an atmospheric boundary for CTP.

Clouds are assumed to fall between the planetary boundary layer top height and the

Trop height. The planetary boundary layer, as defined by AMS (2012a), is the bottom

region of the troposphere that is affected by surface conditions. CO2 Slicing was limited

to above the PBL in order to limit surface effects and issues in the CO2 Slicing algorithm

which may arise from the inversion. The planetary boundary layer top height (PBL) is

typically no higher than 850 hPa, and can be as low as the surface. The PBL can be

found as the first inversion in the temperature profile. Therefore, for the CO2 Slicing

algorithm, the PBL was found by searching the temperature profile between the surface

and 850 hPa for a temperature inversion, where if no inversion exists, then the PBL was

assumed at the 850 hPa. This is mathematically represented as:

$$P_{(PBL)} = \begin{cases} P_{SFC} \rightarrow T(P_{(SFC)}) < T(P_{(SFC+\Delta P)}) \\ P_a \rightarrow T(P_{(a)}) < T(P_{(a+\Delta P)}) \\ P_{850[hPa]} \rightarrow T(P_{(850[hPa])}) \geq T(> P_{(850[hPa]+\Delta P)}) \end{cases}$$

The Trop, according to the AMS (2012b), defines the boundary of the troposphere and

stratosphere. Because of the diametrically different temperature, moisture, and stability

profiles at the troposphere and stratosphere, the Trop is indicated as a caping inversion at the top of the troposphere. Except in the case of tropospheric protrusions, such in the case of overshooting tops, CTP typically occur at or below the Trop. Therefore, the Trop can be found by searching for the lowest height temperature inversion within the upper troposphere. The Trop is latitudinally and seasonally variant, resulting in possible Trop ranges depending on those two variables (Hu and Vallis, 2019). In the tropics and mid-latitude regions, defined here as 60N - 60S, there is limited variability throughout the year. But at the poles, the north 90N - 60N (south 60S-90S) pole has a potentially lower Trop during boreal (austral) summer compared to autumn and spring months, and potentially an even lower Trop during boreal (austral) winter compared to boreal (austral) summer. This is simplified in the table below.

Mid-November to Mid-March

Latitude Range	90N - 60N	60N - 60S	60S - 90S
Trop Range	0 hPa - 375 hPa	0 hPa - 200 hPa	0 hPa - 250 hPa

Mid-March to Mid-May and Mid-September to Mid-November

Latitude Range	90N - 60N	60N - 60S	60S - 90S
Trop Range	0 hPa - 200 hPa	0 hPa - 200 hPa	0 hPa - 200 hPa

Mid-May to Mid-September

Latitude Range	90N - 60N	60N - 60S	60S - 90S
Trop Range	0 hPa - 250 hPa	0 hPa - 200 hPa	0 hPa - 375 hPa

2. Increasing the number of channel pairs from 3 to 4, including a smaller wavenumber

channel pair for upper-level features.

CO_2 Slicing was originally limited to the channels available on HIRS. This limited the

number of available CO_2 absorption to just 4 wavenumbers, or 3 pairs. These channel

pairs were each roughly associated with CTP heights. That is,

HIRS channels 4 and 5 (704 cm^{-1}, 716 cm^{-1}) associated with high (weighting peak around

350 hPa) level CTP

HIRS channels 5 and 6 (716 cm^{-1}, 732 cm^{-1}) associated with mid (weighting peak around

550 hPa) level CTP

HIRS channels 6 and 7 (732 cm^{-1}, 748 cm^{-1}) associated with low (weighting peak around

850 hPa) level CTP

From Menzel et al. (2008), CO_2 Slicing works best at 700 [hPa] or higher, and CO_2

Slicing shows more promise higher up in atmosphere where it can detect upper level

cirrus. Thus, an addition of a fourth, smaller wavenumber would best enhance the CO_2

Slicing algorithm. This was done by including 691.875 cm^{-1}. Additionally, to align with

CrIS channels, 705 cm^{-1}, 715 cm^{-1}, 733.125 cm^{-1}, and 748.125 cm^{-1} were used.

3. Using channel pair groupings, rather than just a singular channel pairs, and IR

window test.

To limit observation noise, 4 wavenumbers surrounding each of the central 4 smaller wavenumbers were used as quality control and to enable CO2 Slicing CTP averaging. The wavenumbers surrounding the central wavenumber were selected at 1.2 cm^{-1} intervals. This was to keep all wavenumbers on the rotational band. Moreover, an IR window test was added as a secondary test and to detect lower level CTP (Menzel, 2009). That is,

CTP Category	Wavenumber 2 ν_2 cm^{-1}	Wavenumbers 1 ν_1 cm^{-1}
High	705	689.375, 690.625, 691.875, 693.125, 694.375
Mid-High	715	702.5, 703.75, 705, 706.25, 707.5
Mid	733.125	712.5, 713.75, 715, 716.25, 717.5
Mid-Low	748.125	730.625, 731.875, 733.125, 734.375, 735.625
Low and SFC	N/A	959.375

The three component equations of the CO2 Slicing algorithm are the CO2 Slicing equation, the IR window test equation, and the optical thickness equation. As with the NCEP Algorithm, a visual representation of CO2 Slicing can be found in Figure 2.2. Below is the CO2 Slicing algorithm protocol:

1. The PBL and Trop are calculated using the 128 analyses pressure levels and the associated ambient atmospheric temperature profiles. Then, an array of $A_2(\nu, P)$ is compiled for each FOV at each 21 CrIS channels listed above (i.e., not including the 959.625 cm^{-1} IR window test channel).
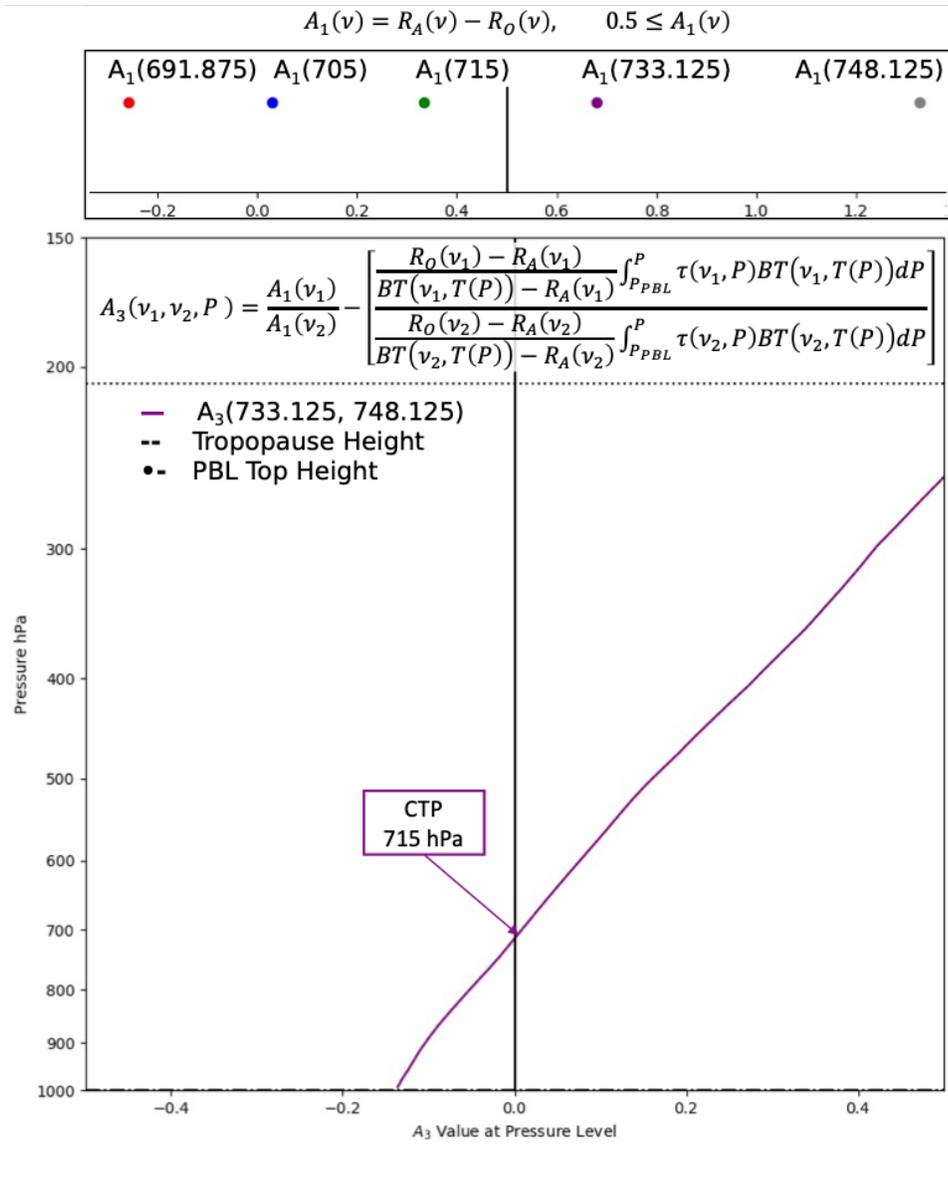
$$A_1(\nu) = R_A(\nu) - R_O(\nu), \qquad 0.5 \leq A_1(\nu)$$

$A_1(691.875)$ $A_1(705)$ $A_1(715)$ $A_1(733.125)$ $A_1(748.125)$

$$A_3(\nu_1, \nu_2, P) = \frac{A_1(\nu_1)}{A_1(\nu_2)} - \frac{\left[\dfrac{R_O(\nu_1) - R_A(\nu_1)}{BT(\nu_1, T(P)) - R_A(\nu_1)} \int_{P_{PBL}}^{P} \tau(\nu_1, P) BT(\nu_1, T(P)) dP\right]}{\left[\dfrac{R_O(\nu_2) - R_A(\nu_2)}{BT(\nu_2, T(P)) - R_A(\nu_2)} \int_{P_{PBL}}^{P} \tau(\nu_2, P) BT(\nu_2, T(P)) dP\right]}$$

— $A_3(733.125, 748.125)$
-- Tropopause Height
•- PBL Top Height

CTP
715 hPa

FIGURE 2.2: CO2 Slicing works by first searching where the assimilation (A) and observation (O) radiances difference (dots above) at spectrally close CO2 absorption wavenumbers are at or above 0.5 radiance. In this example, 733.125 cm^{-1} and 748.125 cm^{-1} work. Then the wavenumber pair are used to calculated the CTP in the CO2 Slicing formula (A_3) as the pressure level closest to 0. For the example, that occurs at 715 hPa.

$$A_2(\nu, P) = \int_{P_{PBL}}^{P} \tau(\nu, P) BT(\nu, T(P)) dP$$

$$A_2(FOV) = \begin{bmatrix} A_2(\nu_{689.375}, P_{Trop}) & A_2(\nu_{690.625}, P_{Trop}) & \ldots & A_2(\nu_{748.125}, P_{Trop}) \\ A_2(\nu_{689.375}, P_{Trop-\Delta P}) & A_2(\nu_{690.625}, P_{Trop-\Delta P}) & \ldots & A_2(\nu_{748.125}, P_{Trop-\Delta P}) \\ \vdots & \vdots & \vdots & \vdots \\ A_2(\nu_{689.375}, P_{PBL+\Delta P}) & A_2(\nu_{690.625}, P_{PBL+\Delta P}) & \ldots & A_2(\nu_{748.125}, P_{PBL+\Delta P}) \end{bmatrix}$$

τ values are simulated from model data. Values of BT are calculated via Planck's

function using the following equation:

$$BT(\nu, T(P)) = \frac{1.191042*10^{-5}*\nu^3}{e^{\left(\frac{1.4387752\nu}{T(P)}\right)}}$$

2. Meanwhile, an additional array is compiled for A_1 at each FOV for the 21 CrIS chan-

nels. Analyses clear radiances, are provided as singular values for each wavenumber,

just as with observed radiance data, making A_1 not pressure depended.

$$A_1(\nu) = R_A(\nu) - R_O(\nu)$$

$$A_1(FOV) = [A_1(\nu_{689.375}) \quad A_1(\nu_{690.625}) \quad \ldots \quad A_1(\nu_{748.125})]$$

3. The last array calculated is for the IR window test. It compares the ambient

temperature profile to the observed BT at a wavenumber sensitive to surface features

($959.375 \ cm^{-1}$). This is done for the full atmosphere, rather than from the PBL

to the Trop, as this test is used to detect any near surface level clouds, as well as

potential identify an upper layer CTP missed earlier. This test can also identify if

a FOV is clear or surface fog by indicating a pressure level at or near the surface.

$N\varepsilon$ will not be calculated quite yet, as the calculated CTP will be required.

$$IR(P_{CTP}) \rightarrow 0 \approx T(P_{CTP}) - BT_O(959.375)$$

$$IR(FOV) = \begin{bmatrix} T(P_m) - BT_O(959.375) = min \rightarrow P_{CTP} = P_m \\ \vdots \\ T(P_2) - BT_O(959.375) = min \rightarrow P_{CTP} = P_2 \\ T(P_1) - BT_O(959.375) = min \rightarrow P_{CTP} = P_1 \end{bmatrix}$$

4. The observed radiance for FOV in a cloud should, ideally, be sufficiently different from the model analyses calculated clear radiance. CO2 Slicing takes this concept to identify a cloud by searching through the analyses and observation difference array, $A_1(FOV)$. This is done by assuming that a 0.5 radiance difference or more indicates a cloud and assuming that if this difference is large enough for one wavenumber it should also be large enough for larger wavenumbers. This cutoff value was selected after a cloud type distribution chart of various CO2 Slicing runs using different cutoff values was compared to a climatology (Menzel, 2009), and the NCEP Algorithm. This is visualized in Figure 2.3. Therefore, the algorithm will search at each channel group for that larger difference, starting with the smallest wavenumber group. If there is no difference above the 0.5 radiance threshold in the first channel group, then the next channel group is searched. The search will stop either when at least one channel in a channel grouping satisfies the cloud detection threshold test or all channel groups have been exhausted.

If a channel group has at least one wavenumber where $A_1(\nu_1) \geq 0.5$, then the CO2 Slicing equation is calculated for all wavenumbers in the group that meet the
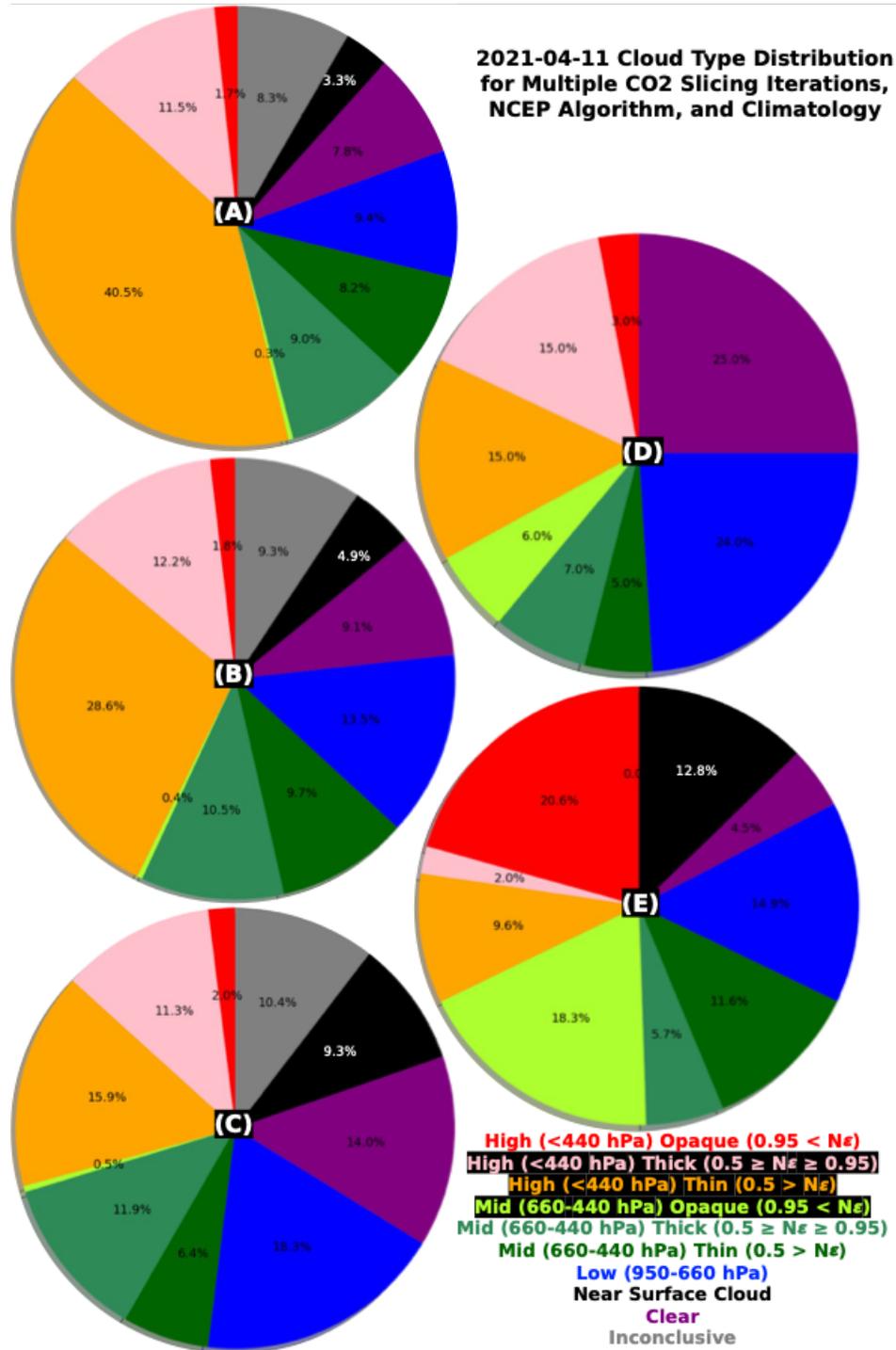
FIGURE 2.3: The distribution of cloud types, defined by CTP and Nε, were plotted for three iterations of CO2 Slicing. The iterations differed by the threshold, at 0.25 (A), 0.5 (B), and 1.0(C). They were compared against for climatology (D) to determine the best match (Warren et al., 1986). NCEP Algorithm (E) distribution included for reference.
    Inconclusive data occurs when CO2 Slicing did not provide a conclusive result.

criteria. If no channel makes $A_1(\nu_1) \geq 0.5$ true in the 4 groupings, then the CO2

Slicing is inconclusive, and the IR window channel test is performed.

$$\begin{bmatrix} \{A_1(689.375)|A_1(690.625)|A_1(691.875)|A_1(693.125)|A_1(694.375) \geq 0.5 \\[6pt] \rightarrow CO_2(\nu_1, 705), \nu_1 = [689.375|690.625|691.875|693.125|694.375] \rightarrow Done \\[6pt] \{A_1(689.375)\&A_1(690.625)\&A_1(691.875)\&A_1(693.125)\&A_1(694.375) < 0.5 \\[6pt] \downarrow \\[6pt] \{A_1(702.5)|A_1(703.75)|A_1(705)|A_1(706.25)|A_1(707.5) \geq 0.5 \\[6pt] \rightarrow CO_2(\nu_1, 715), \nu_1 = [702.5|703.75|705|706.25|707.5] \rightarrow Done \\[6pt] \{A_1(702.5)\&A_1(703.75)\&A_1(705)\&A_1(706.25)\&A_1(707.5) < 0.5 \\[6pt] \downarrow \\[6pt] \{A_1(712.5)|A_1(713.75)|A_1(715)|A_1(716.25)|A_1(717.5) \geq 0.5 \\[6pt] \rightarrow CO_2(\nu_1, 733.125), \nu_1 = [712.5|713.75|715|716.25|717.5] \rightarrow Done \\[6pt] \{A_1(712.5)\&A_1(713.75)\&A_1(715)\&A_1(716.25)\&A_1(717.5) < 0.5 \\[6pt] \downarrow \\[6pt] \{A_1(730.625)|A_1(731.875)|A_1(733.125)|A_1(734.375)|A_1(735.625) \geq 0.5 \\[6pt] \rightarrow CO_2(\nu_1, 748.125), \nu_1 = [730.625|731.875|733.125|734.375|735.625] \rightarrow Done \\[6pt] \{A_1(730.625)\&A_1(731.875)\&A_1(733.125)\&A_1(734.375)\&A_1(735.625) < 0.5 \\[6pt] \downarrow \\[6pt] Refer\ to\ IR\ Window\ Test \end{bmatrix}$$

(a) The case that $A_1(\nu_1) \geq 0.5$ is *true* at least once:

Because analyses datasets are discrete, rather than continuous, there is typ-

ically not an exact point where the two ratios equate. So, the CO2 Slicing

equation works by searching for the closest pressure level where the equation is most true. The pressure level which that is true is assumed to be the CTP. If 1 wavenumber matches the criteria, then the CTP from that one wavenumber is use as truth. If 2 wavenumbers match, a simple average is taken of the calculated CTP. If 3-5 wavenumbers match, then a weighted average is taken, only taking the average of CTP values with 1 standard deviation of the mean. This is visualized in Figure 2.4, and the efficacy of using 5 channels is demonstrated in Figure 2.5. A detailed explanation of O-A plots is provided in 3.1.1. The O-A plot suggests that using the single central channel would limit the number of FOVs that meet the cutoff value. Using the 5 channels, resulting in 31 combinations of wavenumbers used, results in nearly a 20% increase in FOVs used as compared to one, and a 10% increase compared to 3. No significant increase was provided for using above 5 channels, and would result in wavenumbers not sufficiently close spectrally.

This CO2 Slicing CTP value is then compared to the IR window test value. If the CTP from the IR window test is higher up in the atmosphere than from the CO2 Slicing CTP, then the IR window test CTP is selected. Additionally, a further tests based on $N\varepsilon$ is performed to verify that the $N\varepsilon$ is less than 1.3 (allowing for some error) using the CTP as the pressure,

$$N\varepsilon(959.375, P_{CLD}) \leq 1.3$$

However, if this test fails, the FOV is marked inconclusive.

(b) The case that $A_1(\nu_1) \geq 0.5$ is *false* for all wavenumbers:

| 712.5 | 713.75 | 715 | 716.25 | 717.5 |

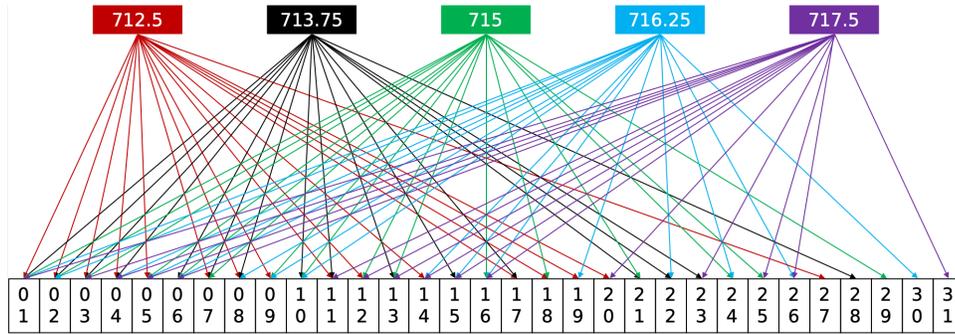| 01 | 02 | 03 | 04 | 05 | 06 | 07 | 08 | 09 | 10 | 11 | 12 | 13 | 14 | 15 | 16 | 17 | 18 | 19 | 20 | 21 | 22 | 23 | 24 | 25 | 26 | 27 | 28 | 29 | 30 | 31 |

FIGURE 2.4: Each CO2 Slicing wavenumber group has 32 combinations of possible solutions. For example, take the wavenumber group with $\nu_2 = 733.125 \ cm^{-1}$. Above are the ν_1 wavenumbers within the group, and below are the 31 combinations. In combination 01, all 5 wavenumber meet the cutoff threshold, so the weighted average of the 5 wavenumbers is calculated. The 32 combination is that no wavenumber meet the cutoff threshold, and CO2 Slicing continues to the next group/step.

The conclusion then **is not** that CO2 Slicing equation did not detect a cloud, therefore the FOV is clear. The conclusion **is** that the CO2 Slicing equation was inconclusive in finding a cloud, and the IR window test is used. The IR window test may provide a CTP provided Nε is acceptable.

If this IR window equation CTP is within the PBL and Trop range, and $A_1(959.375) \geq 0.5$, then the CTP provided is taken as true.

If this IR window equation CTP is very close to the surface and $A_1(959.375) \geq 0.5$, then the FOV has a surface cloud or fog.

If this IR window equation CTP provided and $A_1(959.375) \leq -0.33$ over land or $A_1(959.375) \leq 0.5$ over ocean, then the FOV is marked as clear.

In any other case, the FOV is marked inconclusive.

5. The end result of the CO2 Slicing algorithm, then, is a clear or cloudy classification for each FOV at each of the 22 CrIS wavenumbers. For FOVs with cloudy
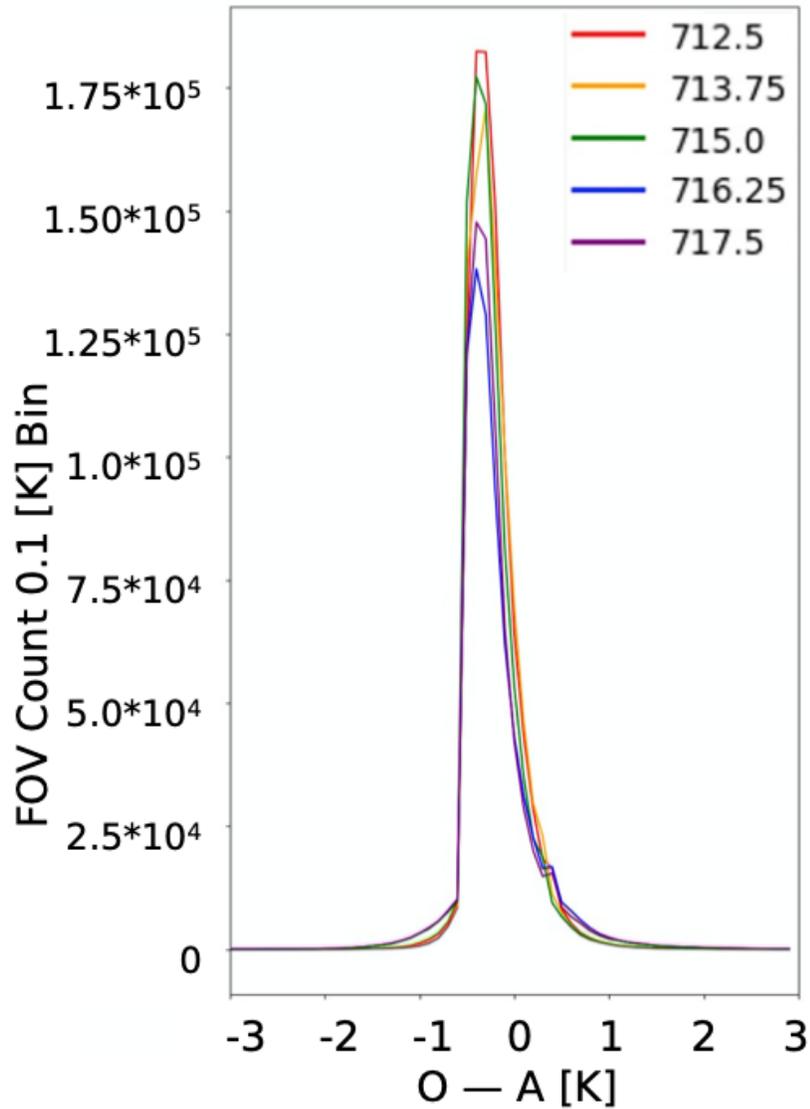
FIGURE 2.5: The utility of using 5 wavenumbers for CO2 Slicing is demonstrate in this figure. Only using wavenumber 715 (green) results in more than 356,000 fewer FOVs used. The bulk of the missing FOVs have O-A values close to 0, as shown by the area under the curve between the wavenumbers 712.5 (red) and 715.

classification at any CrIS wavenumber, a singular CTP and Nε value is calculated.

Note, there are still several CrIS CO2 absorption wavenumbers not used in this version of CO2 Slicing. This suggests that CO2 Slicing could be further adapted to fully optimize the use of CrIS.

2.3.2 Explanation of DR

DR, as described in Smith et al. (2012), works from the fact that small wavenumbers are associated with features higher up in the atmosphere to develop atmospheric profiles. Namely, clear and cloudy trained atmospheric profiles are developed for each FOV. This is done by noting that each wavenumber spectrally peaks at different pressure level, providing a height coordinate, and thus the calculated BT can be used to infer an atmospheric profile. DR is operational on HyperSpectral ReTrieVal (HSRTV) software, hosted by University of Wisconsin-Madison (UW-Madison), Space Science and Engineering Center (SSEC), and JPSS's Community Satellite Processing Package (CSPP) (Weisz, 2020). Dissimilar to the other algorithms, DR on HSRTV develops the two atmospheric profiles from simulated clear radiances via the Principal Component-based Radiative Transfer Model (PCRTM) and historical thermodynamic properties, such as wind and temperature, tendencies. Different orthogonal functions are used for clear and cloud radiance calculations. The coefficients for the functions come from a weighting system based on all CrIS channels $\leq 2400 cm^{-1}$. The coefficients are selected via the observed BT and radiances measured by CrIS, as well as the FOV location and time of year. Like CO2

Slicing, DR runs through 8 height levels for cloudy profile formulation. The height range for the two profiles is 100 hPa - 1000 hPa, bounding CTP classification in that range.

The identification of a cloud is logically parallel to the NCEP Algorithm and CO2 Slicing. That is, a cloud is identified if the clear and cloudy trained profiles diverge at some height. Conceptually this works by assuming above the CTP, the clear and cloudy profiles should coincide. However, at the CTP the profiles should bifurcate, with the cloudy trained profile terminating at a colder BT than the clear profile at 1000 hPa. If the FOV is clear, there should be no divergence of the profiles. The Nε is calculated via the PCRTM.

DR, as with the NCEP Algorithm, does not select channels used in the algorithm specific to the FOV, rather via quality controls as a function of the full input file. However, unlike how the other algorithms provide a unique channel and FOV specific cloudy or clear classification, DR only provides one classification per FOV representing the full atmospheric profile. The end product of DR, then, for each FOV is a clear or cloudy classification, and a CTP and Nε value for cloudy FOVs. HSRTV additionally provides an output array of the channels used in the retrieval with dimensions of CrIS channels $\leq 2400cm^{-1}$. A distinctive feature of DR on HSRTV is the algorithm can also be run using the European Space Agency IR Atmospheric Sounding Interferometer and NASA Atmospheric IR Sounder on the Aqua satellite, broadening the scope of DR's capabilities.

2.3.3 Explanation of ECMWF-CAD

ECMWF-CAD is a software package developed by ECMWF, comprising of an aerosol and a cloud detection component. The cloud detection component is based on the work by McNally and Watts (2003). It uses observed and calculated BT difference at multiple CrIS wavenumbers and a cloud sensitivity ranking of those CrIS wavenumbers to detect clouds. The channels are ranked according the channel height assignment, which was done in this paper via a weighting function derived pressure provided by the analyses. The analyses also provided the clear simulated BT. The observed BT came from CrIS. Because of the channel ranking system, it cannot be assumed that smaller wavenumbers are more sensitive to features higher up in the atmosphere. Additionally, as discussed in the description of the algorithm below, clouds are generally assumed to be between the Trop and PBL.

The McNally and Watts (2003) paper provides ECMWF-CAD with assumed limits on what channels are used, and how many FOVs are classified as clear at various wavenumbers. Between 666.67 cm^{-1} (15 μm) and 714.3 cm^{-1} (14 μm), more FOVs are marked clear than at any other wavenumber range at 40-100% of all FOVs, and from 714.3 cm^{-1} (14 [μm]) to 888.33 cm^{-1} (12 μm) around 5-10% of all FOVs are marked clear. This roughly aligns with the other algorithms.

The objective of ECWMF-CAD is to provide a list of FOVs at each wavenumber that are calculated as clear. While it outputs a binary cloudy or clear classification for each

FOV at each wavenumber, it does not provide a CTP or Nε value for each FOV. A CTP or Nε could be calculated via interoperable input data, but would only work as a proxy, is not automated, and is not as direct as other algorithms.

2.4   Algorithm Outputs and Interoperability

The output of each algorithm is designed for the algorithm's functionality and purpose. This does, however, occasionally cause challenges when comparing algorithms against one another. Data interoperability is required for algorithm comparisons. Interoperability may need to be forced, or was innate. An example of innate interoperability within the scope of this project is the NCEP Algorithm and CO2 Slicing. Both algorithms require the same input data, ensuring that spatial and temporal resolution is conserved. Within the scope of this project, both also output many of the same variables, where the missing data comes from CO2 Slicing only assimilating over 22 channels versus the NCEP Algorithm potential over 431. Interoperability was arranged for ECMWF-CAD and DR with some adjustments. ECMWF-CAD, while requiring the same inputs as the NCEP Algorithm and CO2 Slicing, has latitude and longitude data in a different array dimension as the others, and with less significant figures. Therefore, the NCEP Algorithm and CO2 Slicing had to be indexed to ECWMF-CAD while limiting significant figures and searching for similar coordinate points. DR required a different input file compared to the other algorithms affecting temporal resolution, and restructuring the spatial resolution. This required the NCEP Algorithm and CO2 Slicing FOVs to provide a coordinated perimeter to match the gridded and smaller resolution of DR.

Additionally, ECWMF-CAD did not output CTP or Nε information, and DR didn't output a cloudy or clear classification for each wavenumber. Therefore, only certain output variables of each algorithm were compared. That is, only CTP and Nε values from CO2 Slicing and DR were compared against the NCEP Algorithm. And only cloudy or clear classification for each wavenumber from CO2 Slicing and ECMWF-CAD was compared against the NCEP Algorithm.

2.5   Simple Case versus Complex Case Method

There are several potential challenges in working on a global scale as it pertains to IR cloud detection. Broadly speaking, surface IR ε varies drastically over different regions in the world, and can impact the boundary conditions of the algorithm (Li et al., 2013). The algorithm may misclassify the surface as clouds when the surface has ε values considerably less than 1 (especially over desert sand, snow, and ice). Regions with multiple topography types over a small distance, such as land-sea boundaries or forests, require oversimplification to represent a complex scene with one ε value. Surface ε also assumes a smooth surface, so rough surfaces such as forest, mountains, or ice have complicated radiative scattering routines. Additionally, cloud detection via satellite remote sensing comes with its own challenges. Satellite scan from the top down, with stronger retrieval accuracy higher up in the atmosphere than the surface, father away from the satellite. Using a scanning method results in poorer resolution than nadir view for FOVs not at nadir—however, not drastically for CrIS. And daylight is required when comparing IR methods against visible satellite imagery.

A simple case using an IR cloud detection algorithm would seek to limit this variability. This case would come from limiting the FOVs within a 24-hour test day to just those over ocean. The ocean is a relatively smooth surface, is more uniform than land, and has approximately the same constant ε throughout the entire body. To limit ice and snow effects, polar regions (between latitude 60N-60S) would be eliminated. A test day around an equinox should be selected to further limit seasonal effects, such as snow, and hemispherical difference. For visual confirmation and comparison of cloud truth via VIIRS, only FOVs with solar zenith angles $\leq 84°$ would be used. This simpler case would demonstrate the natural capability of an algorithm.

However, to test the robustness and global capabilities of an algorithm, a more complex case could be used. This complex case would not limit any parameterization of the data, and would come for a different 24-hour test day. If the results of this complex, global case are very similar to the simple, idealized case, then it could be assumed that the algorithm has limited sensitivity to topographic, temporal, and latitudinal variability. And to ensure reproducibility, reliability, and accuracy of the results, multiple complex cases could be compared to the simple case.

Therefore, a simple case and multiple complex cases were studied in this project. The four test days used were selected as visual VIIRS imagery implied a robustness of cloud quantity, types, and global distribution. Cloud types were categorized by CTP and Nε, where:

$$N\varepsilon$$

Optically Thin	$N\varepsilon < 0.5$
Optically Thick	$0.5 \leq N\varepsilon \leq 0.95$
Optically Opaque	$N\varepsilon > 0.95$

CTP

High-Level	50 hPa – 440 hPa
Mid-Level	440 hPa – 660 hPa
Low-Level	660 hPa – surface

For the simple case, April 11, 2021 was used, whereas the complex cases days selected were October 10, 2020, January 2, 2021, April 11, 2021, and July 30, 2021. Each of the algorithms were run for the simple case day. Then interoperable outputs from the algorithms were compared to one another via objective assessment techniques discussed in the results section. Only the best candidate algorithm alongside the NCEP Algorithm were run for the complex cases. The conclusion section details suggestions from the results to improve the NCEP Algorithm.

Results

3.1   Plot Types Explained

Several types of plots were used to investigate and explain the accuracy and viability of the algorithms. Some of them are typical atmospheric plots, such as CTP and Nε point plots. Other plots are more specialized to the topic at hand. Therefore, for clarification and simplification purposes, a description of specialized plots used is detailed in this section.

Note, each FOV is represented by a data point. Scatterplots were selected over the typical contour plots for two reasons. Firstly, the output data was spatially and temporally discrete. So while two points may be spatially close, they may be temporally distant, or vice versa. Therefore, linear interpolation can't be used. Secondly, the end product requires discrete point data.

3.1.1   Observation Minus Analyses [O-A] Distribution Plots

Observation minus analyses model BT distribution plots (henceforth O-A plots) are used to count the number of accurately identified clear FOVs and test error type. O-A plots graph the quantity of FOVs identified by the algorithm as clear in 0.1° bins. Bins are classified by the difference of the FOV analyses calculated clear BT and FOV observed
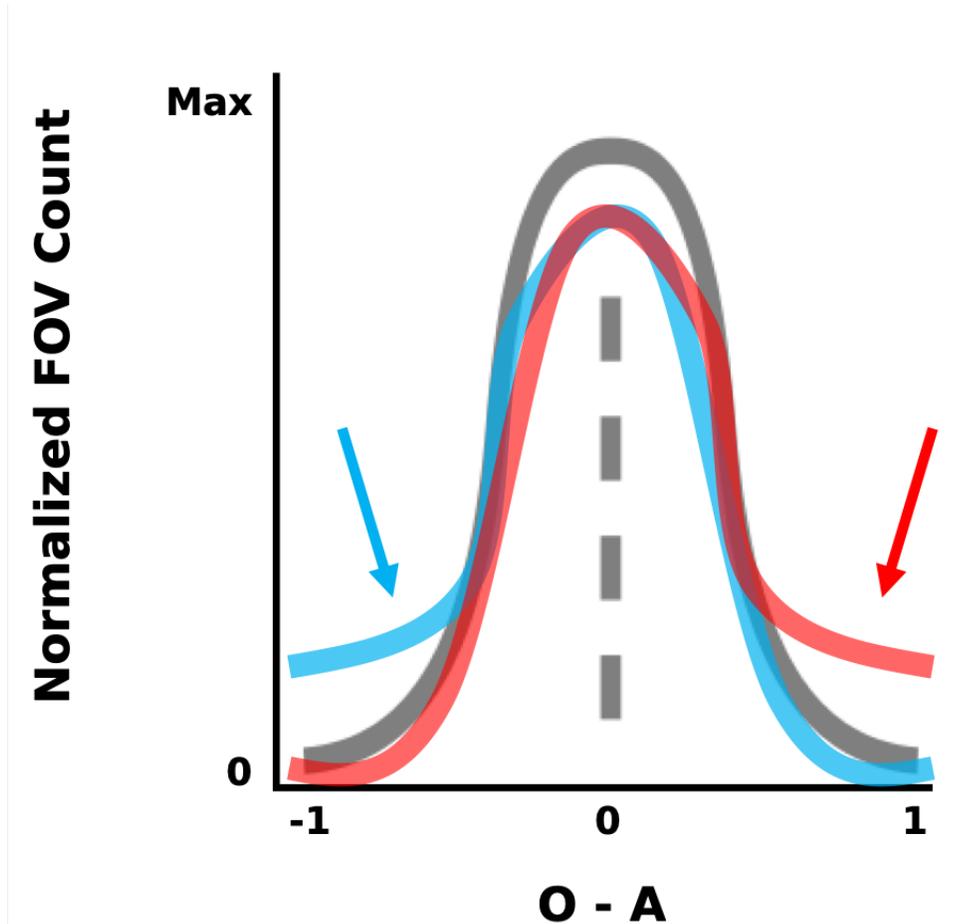
FIGURE 3.1: On the x-axis is the difference between the FOV clear analysis BT (A) and CrIS observed BT (O). On the y-axis is the number of FOVs classified by an algorithm as clear normalized to a gaussian curve. The black curve is from an idealized solution, that is symmetrical on 0, with a tall and skinny distribution. The blue (red) curve demonstrates a distribution that has a cold (warm) tail, identified by the blue (red) arrow. Note, this is a theoretical example.

BT at a given wavenumber. If the observed BT is very close to the clear analyses BT (a difference close to 0), the FOV is almost certainly clear. This is shown in Figure 3.1.

Ideally, the distribution should be Gaussian and centered on 0. A tall distribution at 0 indicates a large number of correctly identified clear FOVs. Any peak skewed from 0 may indicate an algorithm with a bias error. A relatively small number of FOVs

centered on 0 indicates the algorithm is potentially not using viable clear FOVs, or a particularly cloudy retrieval. A skinny and symmetrical curve indicates that any errors are statistically random. Deviations from a symmetrical curve include a cold tail, a warm tail, double peaks, and wide distributions. A cold tail occurs when several FOVs classified clear have analyses BT much warmer than observed BT. This likely indicates the algorithm misclassified these cloudy FOVs as clear. A warm tail occurs when several FOVs classified clear have analyses BT values much colder than observed BT. This likely indicates the global model temperatures have a cold bias. Double peaks typical indicate a false clear signature. For example, FOVs with surface clouds may algorithmically get classified as clear, but still have O-A values reminiscent of cloudy FOVs at large (near surface) wavenumbers. Wide distributions may indicate the algorithm is classifying FOVs clear with lower certainty of clear. Though note that global model, analyses, CrIS, or random errors can't always be isolated and diagnosed.

Therefore, a reliable algorithm will have a symmetrical distribution and a relatively large number of FOVs with a 0 difference. The purpose of O-A plots was to demonstrate the algorithm's accuracy of the binary cloudy or clear classification of the FOVs at each wavenumber. This verification was used to both compare algorithms against one another by selecting the algorithm with the best fitted distribution that could then be used as a proxy for observation truth.

3.1.2   Plots from Confusion Matrices

Confusion matrices (also called comparison matrices) are used to identify algorithm agreement with another algorithm or observation truth of binary characteristics. This is best described by this table, assuming Algorithm A is truth and Algorithm B is predictive:

	Algorithm A Clear	Algorithm A Cloudy
Algorithm B Clear	True Positive (+T)	False Positive (+F)
Algorithm B Cloudy	False Negative (-F)	True Negative (-T)

For this project, rather than identifying one algorithm as truth, the NCEP Algorithm was determined as Algorithm A, and Algorithm B was one of the other algorithms. Furthermore, rather than +F and -F or +T and -T, FOVs were classified as contrasting or comparable. FOVs that contrasted were then investigated. A FOV where the other algorithm disagreed with the NCEP Algorithm and identified a cloud could be a cloud affected FOV; a FOV identified as clear from the other algorithm could be an additional FOV that could be assimilated.

Aside from reporting the raw FOV counts, there were several ways to use the information confusion matrices. Visualizing was useful in recognizing patterns where the NCEP Algorithm contrasted with other algorithms. This was done by plotting FOV confusion matrix classifications using 4 distinct colors representing each case. ECMWF-CAD or CO_2 Slicing compared to the NCEP Algorithm were plotted at various wavenumbers.

While the full atmospheric clear or cloudy classification were plotted for DR or CO2 Slicing compared to the NCEP Algorithm. Confusion matrices information was also applied to general plots depending on the classification. For example, 4 different O-A plots were made for each comparable and contrasting type.

3.2 Simple Case Results

As a reminder, the simple case was classified as:

- Day only FOVs (where solar zenith angle was $\leq 84°$) for colocated VIIRS spatial and temporal interoperability

- Ocean only FOVs to limit land surface emissivity effects

- FOVs between 60N and 60S latitude to limit ice and snow effects

- April 11, 2021, which has several clouds and cloud types, was used to limit seasonal effects (near an equinox)

CO2 Slicing, ECMWF-CAD, and the NCEP Algorithm output binary cloudy or clear classifications for all FOVs at several CrIS wavenumbers. The algorithms can only output this classification for input wavenumbers. That is, the NCEP Algorithm and ECMWF-CAD have a classification for every input wavenumber, and CO2 Slicing only has outputs for wavenumbers listed in 2.3.1. Therefore, as an initial test, only those 22 CO2 Slicing wavenumbers were used in the simple case comparison. A set of O-A plots were used
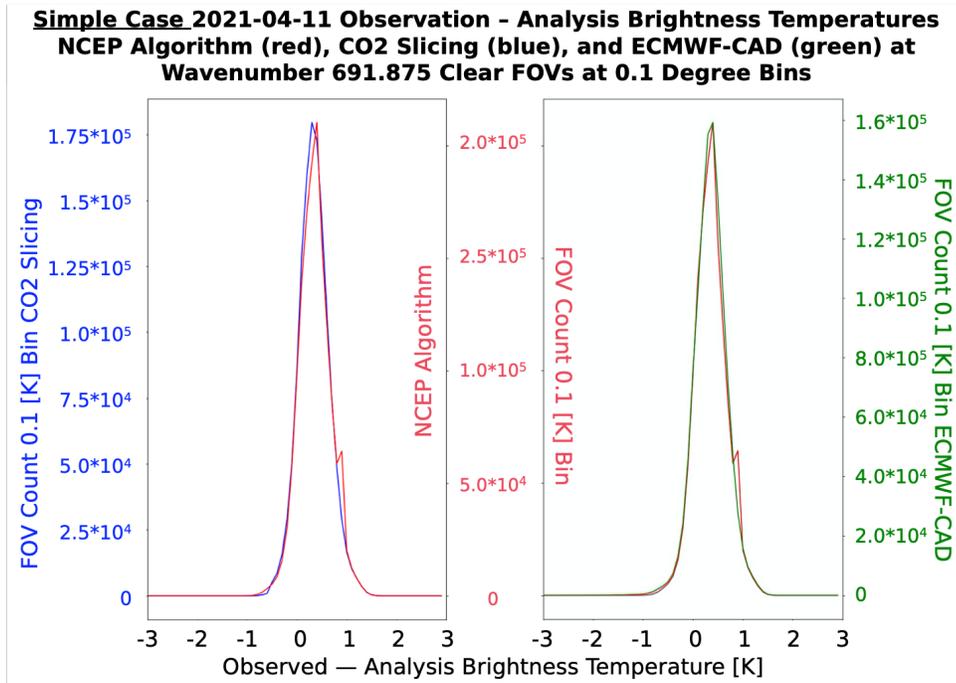
FIGURE 3.2: For the simple case test, i.e., only daylight, ocean, 60N-60S FOVs. O-A distribution plots are plotted using the central CO2 Slicing wavenumber 691.875 cm^{-1}. The NCEP Algorithm (red) was compared to ECMWF-CAD (green) and CO2 Slicing (blue). They are shown side by side for additional CO2 Slicing and ECMWF-CAD comparison. This is for all FOVs in the 24-hour period. For CO2 Slicing $\nu_1 = 691.875\ cm^{-1}$.

to compare all three algorithms. The main CO2 Slicing wavenumbers were included as 691.875 cm^{-1} (Figure 3.2), 705 cm^{-1} (Figure 3.3), 715 cm^{-1} (Figure 3.4), 733.125 cm^{-1} (Figure 3.5), 748.125 cm^{-1} (Figure 3.6), plus the IR Window Test wavenumber 959.375 cm^{-1} (Figure 3.7).

Indicating some random error (noise) at 705 cm^{-1} and 715 cm^{-1}, the distribution of the NCEP Algorithm O-A plots were mostly symmetric. Similarly, CO2 Slicing only had one distribution that was not symmetric on 0 at 748.125 cm^{-1}. ECMWF-CAD, however, had a cold tail starting at 715 cm^{-1}. This cold tail persisted and grew more prominent
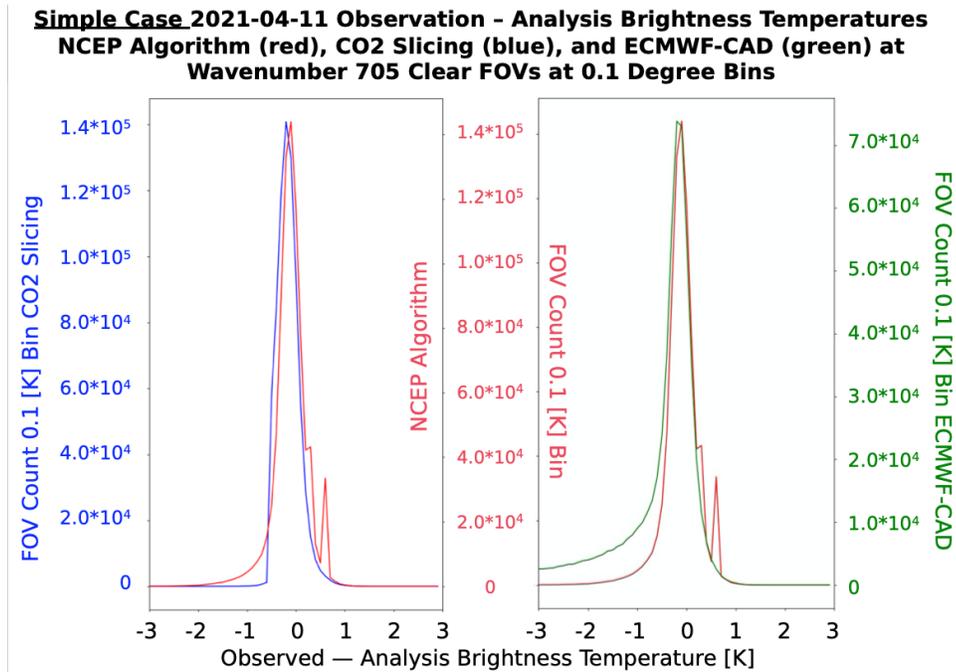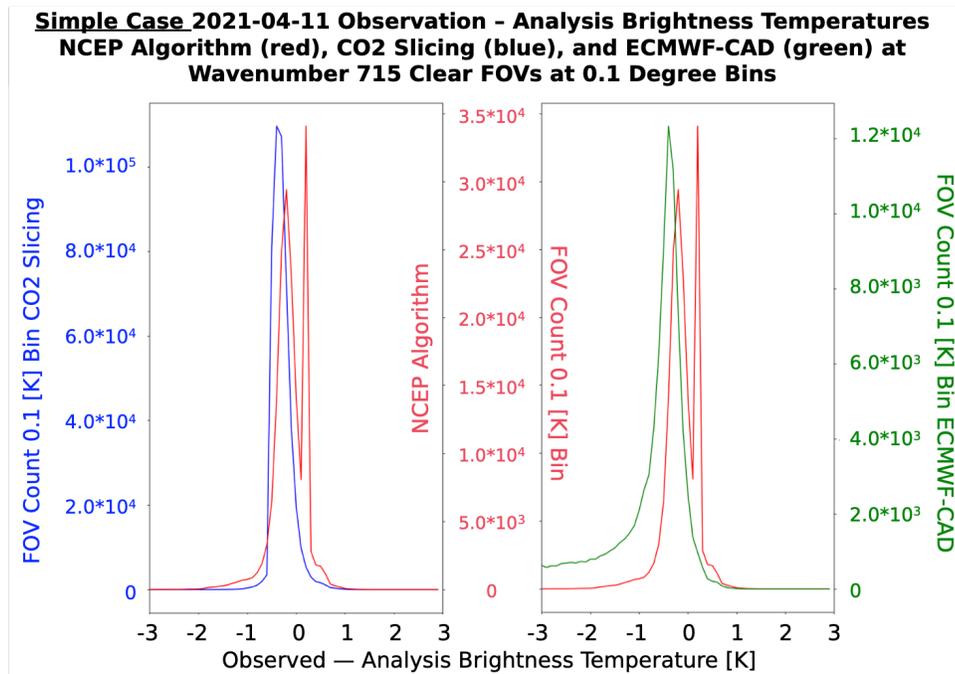
FIGURE 3.3: As with Figure 3.2, this is the O-A plots for 705 cm^{-1}. The NCEP Algorithm (red) was compared to ECMWF-CAD (green) and CO2 Slicing (blue). For CO2 Slicing ν_1 or $\nu_2 = 705$ cm^{-1}.

throughout the remaining wavenumbers. The count of clear FOVs from ECMWF-CAD was also consistently lower than the NCEP Algorithm and CO2 Slicing. The highest peak value for ECMWF-CAD, which was $1.6 * 10^5$ for 691.875 cm^{-1}, was still $1.5 * 10^4$ less than CO2 Slicing at the same wavenumber. This was more pronounced at 705 cm^{-1}, where ECMWF-CAD had a peak value half that of the NCEP Algorithm and CO2 Slicing. Moreover, at 959.375 cm^{-1} the ECMWF-CAD peak value around 0 was more than 8 times less than the NCEP Algorithm and CO2 Slicing. It could be that our use of ECMWF-CAD was not optimal, resulting in an underperformance of the algorithm compared to CO2 Slicing or the NCEP Algorithm. In the simple case, the ECMWF-CAD was deemed less likely to improve the NCEP Algorithm than CO2 Slicing. ECMWF-CAD was further
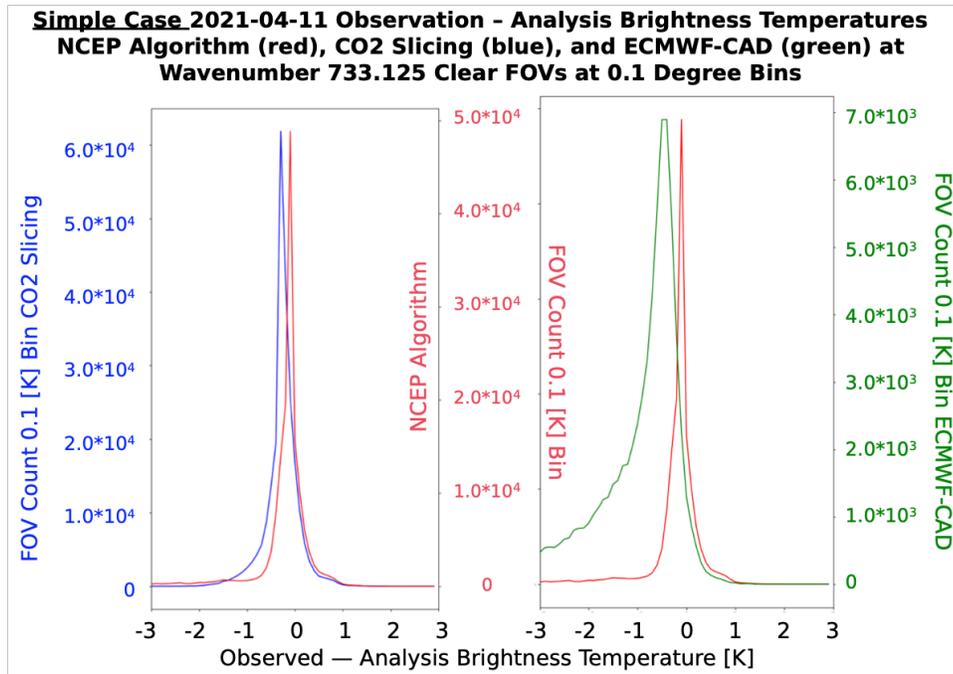
FIGURE 3.4: As with Figure 3.2, this is the O-A plots for 715 cm^{-1}. The NCEP Algorithm (red) was compared to ECMWF-CAD (green) and CO2 Slicing (blue). For CO2 Slicing ν_1 or $\nu_2 = 715$ cm^{-1}.

compared to the NCEP Algorithm in the complex case for the April day.

Conversely, CO2 Slicing and the NCEP Algorithm could be compared in more depth. Comparison of distribution shapes and clear FOV peak counts were used as indicators of whether CO2 Slicing could improve the NCEP Algorithm. The distribution shape of both O-A plots were similar and symmetric, but CO2 Slicing more sharply confined indications of a cold tail as the wavenumbers increased. At 691.875 cm^{-1} and 705 cm^{-1}, CO2 Slicing and the NCEP Algorithm had comparable peak values, with less than 15% difference. At 715 cm^{-1}, the number of near certain clear FOVs detected by CO2 Slicing was still about 25% higher than the NCEP Algorithm (Note, there is a plotting artifact for the NCEP Algorithm 715 cm^{-1}). At 733.125 cm^{-1}, CO2 Slicing also detected 20% more clear FOVs
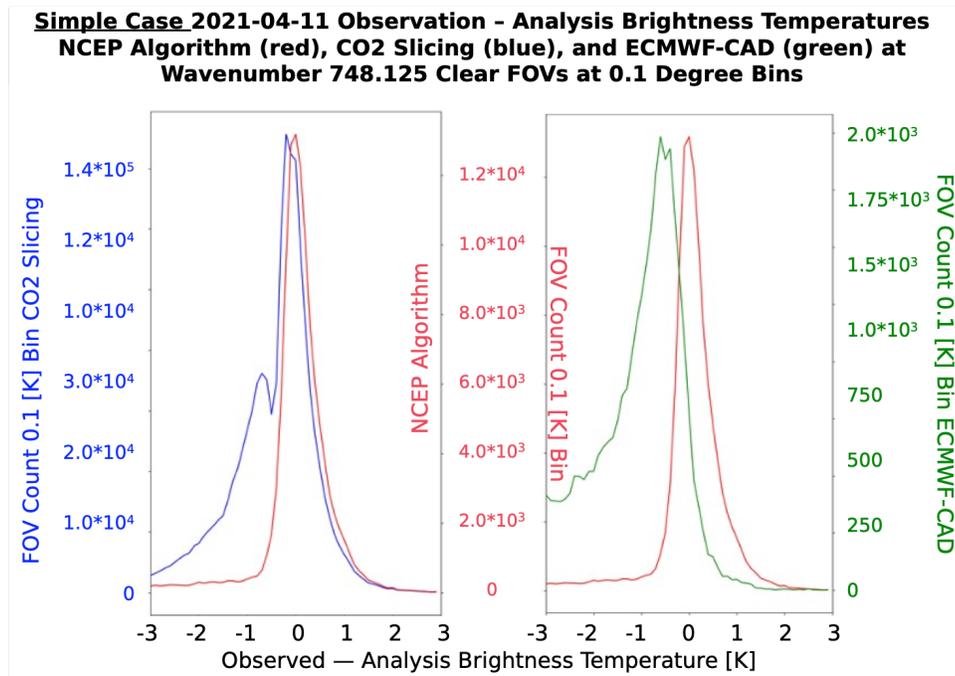
FIGURE 3.5: As with Figure 3.2, this is the O-A plots for 733.125 cm^{-1}. The NCEP Algorithm (red) was compared to ECMWF-CAD (green) and CO2 Slicing (blue). For CO2 Slicing ν_1 or $\nu_2 = 733.125$ cm^{-1}.

than the NCEP Algorithm. Lastly, CO2 Slicing and the NCEP Algorithm performed similarly for wavenumbers lower in the atmosphere. The NCEP Algorithm developed more of a cold tail at this wavenumber. This cold tail became more pronounced with the complex case.

3.3 Complex Case Results

The idea of using the simple case was to perform a test in the most simplistic conditions for cloud detection. The complex cases tested the full capabilities of the algorithms, that is, to test if the algorithms could work well for all surface types (ocean, land, ice, etc.) and year-round. First this was done using the simple case test day. Then reproducibility

Simple Case 2021-04-11 Observation – Analysis Brightness Temperatures NCEP Algorithm (red), CO2 Slicing (blue), and ECMWF-CAD (green) at Wavenumber 748.125 Clear FOVs at 0.1 Degree Bins

FIGURE 3.6: As with Figure 3.2, this is the O-A plots for 748.125 cm^{-1}. The NCEP Algorithm (red) was compared to ECMWF-CAD (green) and CO2 Slicing (blue). For CO2 Slicing $\nu_2 = 748.125$ cm^{-1}.

of results was tested by using the October 2020, January 2021, and July 2021 test days. Note that these 4 test days do not necessarily represent every facet of the algorithms or test every condition or variable, but it provided sufficient insight into the accuracy of the algorithms.

3.3.1 Visual Review Analysis

The first approach in analyzing the algorithms globally was a visual review of the April complex case day. This started by plotting the calculated CTP for CO2 Slicing, DR, and the NCEP Algorithm (see Figure 3.8). ECMWF-CAD did not provide a CTP value, and thus was not plotted. The CTP plots were compared with each other and the VIIRS
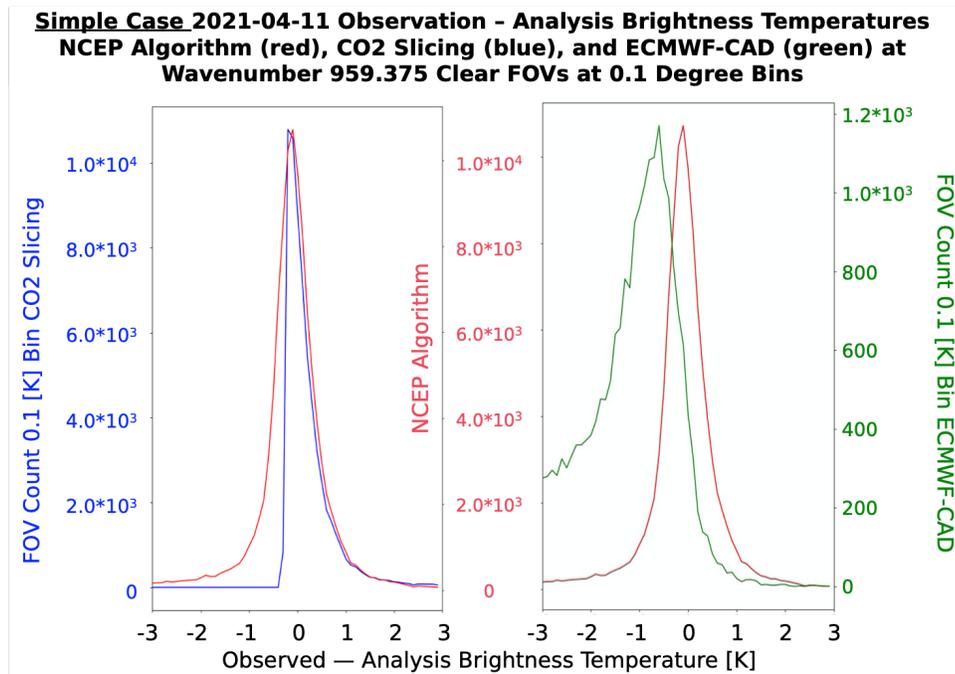
FIGURE 3.7: As with Figure 3.2, this is the O-A plots for the IR window wavenumber of 959.375 cm^{-1}. The NCEP Algorithm (red) was compared to ECMWF-CAD (green) and CO2 Slicing (blue).

24-hour visual composites using synthesized true color (see Figure 3.9). This data came from a NASA database (EOS, 2022), which plotted the data via an equirectangular map projection system. For consistency, all algorithm CTP plots used FOVs within the 24-hour time frame and were plotted using the same projection system, scale, and pressure range (0-1000 hPa). Note, this projection system does distort a FOV from satellite areal size to Python plotted size. The size of the datapoints plotted were similar in scale to the FOV resolution at nadir at the tropics. CTP datapoint size remains roughly the same plots using the same datapoint size for FOVs in the poles and the in the tropics, despite true spatial differences in those regions due to the projection system. Also note, due to the large temporal scale, there may be overlap in CTP values in the plots. This effects

the number of perceived clear FOVs in a visual display. This is addressed using other plots such as O-A plots.

Additionally, to contrast between certain surface types, an edited version of the VIIRS image was developed by using a 400% color saturation correction. For example, this forced surfaces such as ice to be visually distinguished from similarly appearing clouds, enhancing the accuracy of determining observed clear sky over polar regions.

There are a few general comments concerning the CTP plots. The NCEP Algorithm, DR, and CO2 Slicing all detected mainly higher-level CTP for tropical regions. This is typical for 30N-30S (Warren et al., 1986). CO2 Slicing and DR CTP values for FOVs over ocean generally agreed in mid-latitudes. For example, look at eastern Great Australian Bight (130E to 140E and 30S to 45S). CO2 Slicing calculated CTPs around 800-700 hPa. However, the NCEP Algorithm calculated clouds in this region around 650-550 hPa. The largest disparities between CTP values in all three algorithms were over polar latitudes and land. Although, there were regional differences globally.

For regions with discrepancies in the CTP calculations, VIIRS was compared to algorithm CTP plots. In this comparison, there were several regions which make the case that CO2 Slicing might improve the NCEP Algorithm, more than DR, as demonstrated by the better representation of the VIIRS observation. Three regions exemplify this.

Region one is the broader Indian Ocean around Western Australia (105E to 140E and 25S to 45S). At about (135E, 45S), VIIRS appears clear of clouds. Just northwest of this
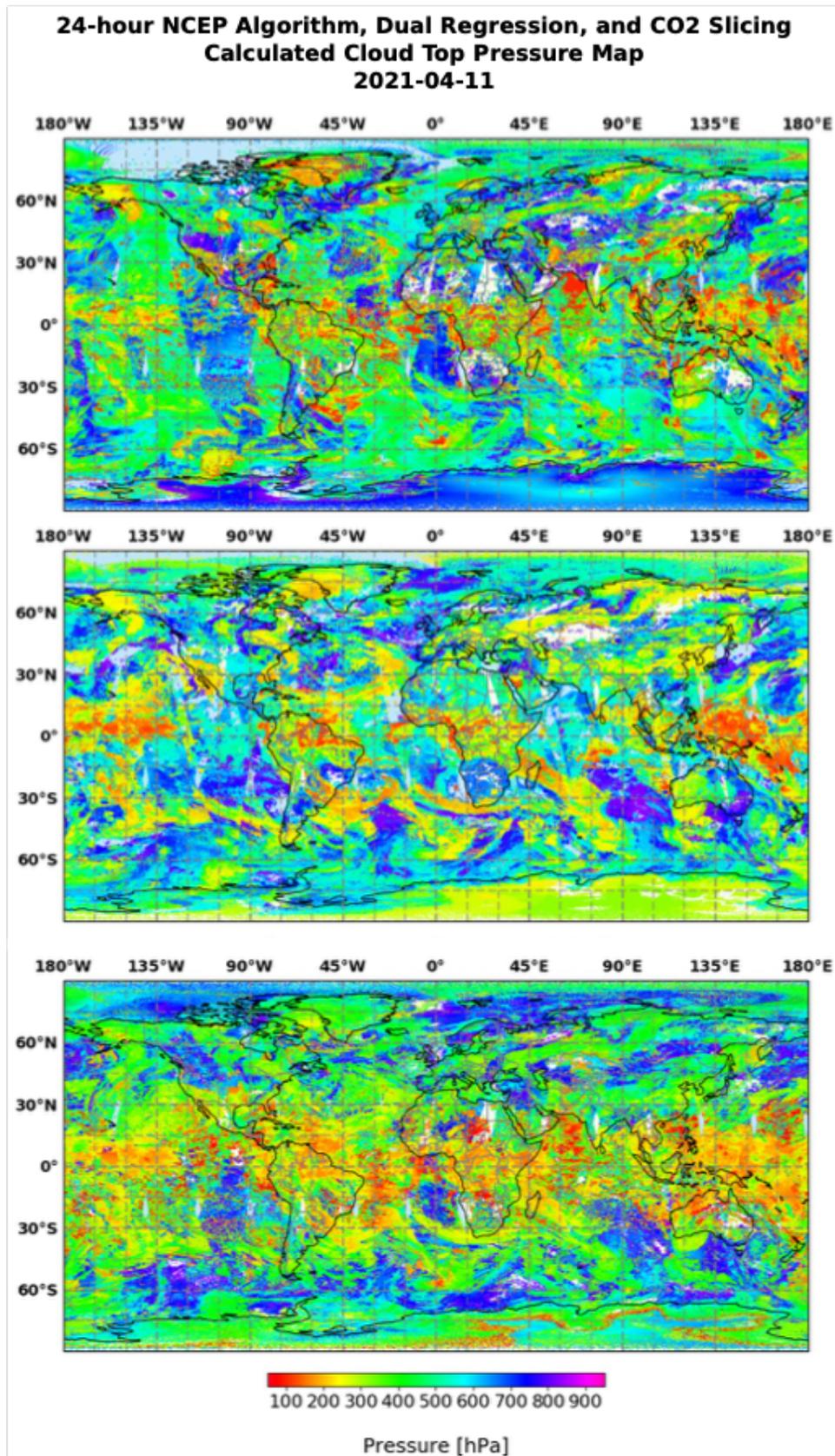
FIGURE 3.8: For FOVs that are cloudy, the NCEP Algorithm (top), DR (middle), and CO2 Slicing (bottom) calculates a CTP. They all have been plotted with the same color bar provided below.
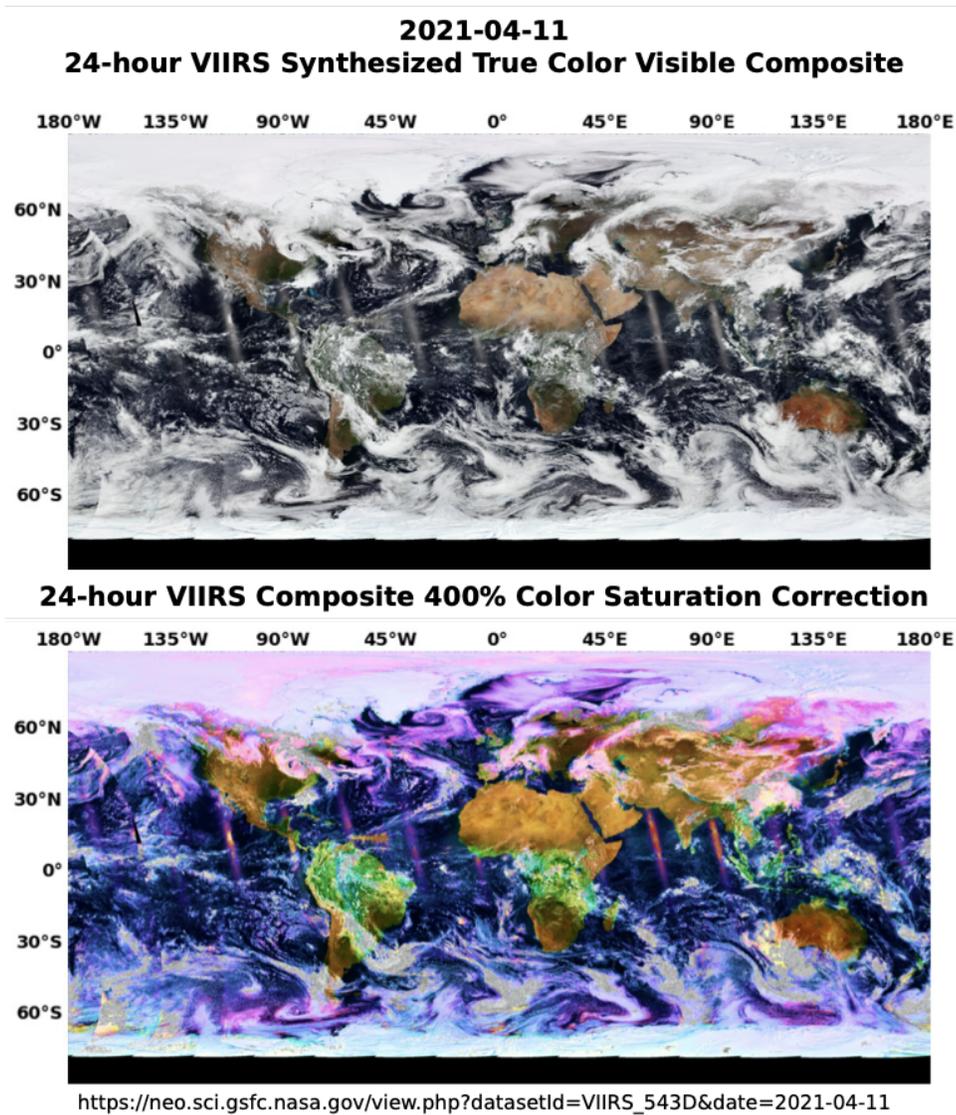
2021-04-11
24-hour VIIRS Synthesized True Color Visible Composite

24-hour VIIRS Composite 400% Color Saturation Correction

https://neo.sci.gsfc.nasa.gov/view.php?datasetId=VIIRS_543D&date=2021-04-11

FIGURE 3.9: The 24-hour synthesized true color visible composite from VIIRS were provided by a NASA database. VIIRS was used for visual confirmation and analysis purposes. For added contrast between clouds and surfaces, an edited version of the original composite was made by enhancing the color saturation 400% (bottom).

is a region of scattered small, cloud (perhaps cumulus). The NCEP Algorithm and DR differ regarding the cloud cover in this region. The NCEP Algorithm fully classifies this region as mid-level clouds. While, DR classified this region as clear. Yet, CO_2 Slicing correctly classifies it clear where clear sky is seen in VIIRS, and cloudy where VIIRS appeared cloudy.

Moving west, toward approximately (105E, 35S), VIIRS appears clear again. However, this time DR classifies this region as lower-level clouds. The NCEP Algorithm and CO_2 Slicing both identify the region as clear, but the NCEP Algorithm extent of clear is much smaller than what appears with VIIRS. CO_2 Slicing displays an appropriate extent of clear FOVs, which is consistent with the clear sky viewed with VIIRS.

The second region is a near polar region south of Greenland, bounded by 75W to 30W and 60N to 45N. The VIIRS image slightly detects some clear FOVs within a mostly cloudy region. The cloud structures are enhanced in the 400% color saturated version, and highlights the possibility of upper-level clouds in the region. DR identified this region mostly cloud free. The NCEP Algorithm indicates a few FOVs with upper-level clouds, as well as a few clear FOVs. CO_2 Slicing identifies more FOVs clear and more upper-level CTP than the NCEP Algorithm, in agreement with the VIIRS image. CO_2 Slicing also captures the complex multileveled cloud scene that the observation figure presumably displays.

The third region, bounded by 180W to 160W and 30N to 15N, compares detection capabilities of upper level optically thin cirrus. Optically thin cirrus, as the name suggests,

are not easily detected by visible imagery. Aside from sun glint on the unedited VI-IRS image, the region could be identified as clear. However, using the enhanced 400% color saturated version, there are several structures that suggest the presence of clouds. The NCEP Algorithm will not detect optically thin clouds, and only identifies the more opaque upper level clouds. The other FOVs within this region are identified as mid-level clouds. DR identifies some clear FOVs, but for the most part classifies these FOVs as mid to lower-level clouds. CO_2 Slicing, again, properly detects what VIIRS imagery suggests. The dominate cloud level CO_2 Slicing suggests for the FOVs is upper level. Where applicable, CO_2 Slicing classifies FOVs clear or classifies FOVs in the mid-atmosphere.

Therefore, at least for this one case study, there is good initial evidence that CO_2 Slicing might improve the NCEP Algorithm. And while DR was, for the most part, on par with CO_2 Slicing, these select regions suggest that CO_2 Slicing may provide a more accurate CTP classification than DR.

3.3.2 FOV Binary Classification Analysis

Two approaches were used to quantitatively test the capabilities of CO_2 Slicing, ECMWF-CAD, and the NCEP Algorithm for the April day complex case. The first compared ECMWF-CAD to the NCEP Algorithm in a more isolated way than used in the simple case. This was done via a distribution of clear FOVs on the full spectrum of wavenumbers. The second compared the results of the simple case to the complex case by using the same plots as in the simple case.
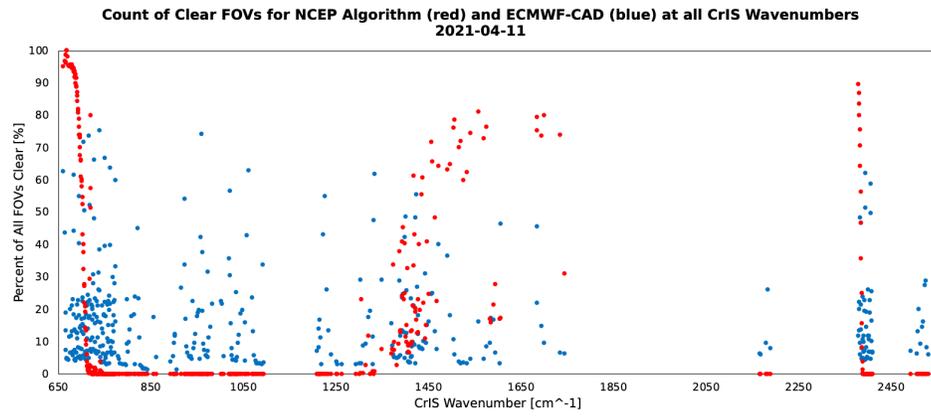
FIGURE 3.10: Plotted are the NCEP Algorithm (red) and ECMWF-CAD (blue) percent of FOVs that are clear at each wavenumber. About 76 of 431 the NCEP Algorithm wavenumbers are more than 60% clear FOVs. That same count is only 13 of 431 for ECMWF-CAD.

As the output was binary, i.e., cloudy or clear, it can be presumed that the sum of all FOVs classified clear plus all FOVs classified cloudy by ECMWF-CAD or the NCEP Algorithm within a 24-hour period at a wavenumber equals the total sum of all FOVs output by an algorithm. Thus, if the majority of the FOVs are clear, then the wavenumber can be considered a clear channel, and vice versa. For a quantitative metric, if a wavenumber has more than 60% clear FOVs, then the wavenumber is considered clear. The percent of clear FOVs identified by the two algorithms at each wavenumber is shown in Figure 3.10.

One way ECMWF-CAD could demonstrate a potential to improve the current NCEP Algorithm would be to identify more clear wavenumbers. Both algorithms used 431 wavenumbers. The NCEP Algorithm considered 17.6% (76/431) wavenumbers clear. This was only 3% (13) for ECMWF-CAD. Lowering the 60% clear FOVs threshold to 50%, ECMWF-CAD still fell short of the NCEP Algorithm at 5.3% compared to 19.7%. Only two wavenumbers coincided with the NCEP Algorithm and ECMWF-CAD at 50% clear:

661.25 cm^{-1} and 683.125 cm^{-1}. The other 21 wavenumbers ECMWF-CAD identified 50% clear could potentially improve upon the NCEP Algorithm. Moreover, of those 21 wavenumbers, 4 overlapped with wavenumbers used in CO2 Slicing (694.375 cm^{-1}, 706.25 cm^{-1}, 717.5 cm^{-1}, and 959.375 cm^{-1}).

However, it cannot be assumed that the FOVs identified by either algorithm are actually clear. Therefore, O-A plots were employed for several wavenumbers. A set of O-A plots were used to compare ECMWF-CAD and CO2 Slicing. This was done at the first three ECMWF-CAD 50% clear wavenumbers that match CO2 Slicing (Figure 3.11). 959.375 cm^{-1} was not included in this set as it was included in the second set. The second set of O-A plots were used to compare all three algorithms to each other and the simple case. As with the simple case, the O-A plots for CO2 Slicing wavenumbers were included for 691.875 cm^{-1} (Figure 3.12), 705 cm^{-1} (Figure 3.13), 715 cm^{-1} (Figure 3.14), 733.125 cm^{-1} (Figure 3.15), 748.125 cm^{-1} (Figure 3.16), and 959.375 cm^{-1} (Figure 3.17).

ECMWF-CAD and CO2 Slicing both execute fairly accurate clear FOV classification at smaller wavenumbers (sensitive primarily in the upper troposphere). At 694.375 cm^{-1}, for example, ECMWF-CAD and CO2 Slicing had O-A symmetrical distributions on 0; ECMWF-CAD did detect more FOVs clear, where ECMWF-CAD detected around $5*10^4$ more FOVs than CO2 Slicing at the peak. But going farther into the atmosphere, CO2 Slicing and ECMWF-CAD switched results. CO2 Slicing detected more FOVs clear centered at 0 than ECMWF-CAD. Additionally, the ECMWF-CAD O-A plots had a less symmetrical distribution compared to CO2 Slicing, resulting in a cold tail. Starting as
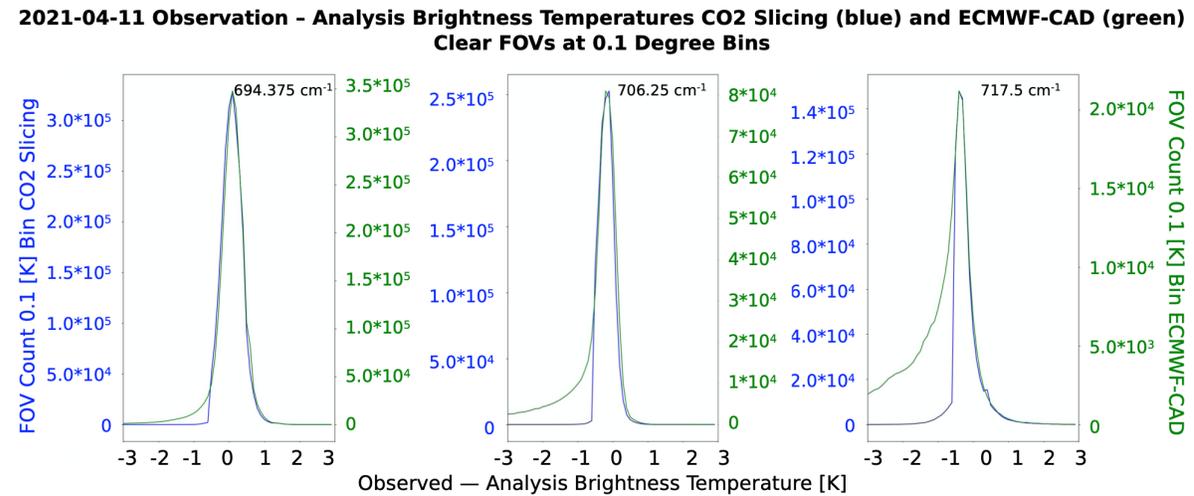
FIGURE 3.11: These O-A plots compares CO2 Slicing (blue) with ECMWF-CAD (green) wavenumbers that had 50% or more clear FOVs. On the left O-A plot was for 694.375 cm^{-1}, center 706.25 cm^{-1}, and right is 717.5 cm^{-1}. These are the ν_1 value for CO2 Slicing.

low as 705 cm^{-1}, there was a cold tail in the ECMWF-CAD curve. This was particularly significant for the wavenumbers which ECMWF-CAD classified as mostly clear FOVs. It was evident from the O-A plot that ECMWF-CAD was possibly detecting a significant percent of these potentially cloudy FOVs as clear. Therefore, there was a low certainty that the wavenumbers were truly 50%+ clear. Conversely, CO2 Slicing maintained a relatively symmetric distribution at nearly all wavenumbers. The number of high likelihood clear FOVs was nearly one order of magnitude greater with CO2 Slicing than ECMWF-CAD for 717.5 cm^{-1}, and 5 times more for 715 cm^{-1}. CO2 Slicing also detected more FOVs clear than the NCEP Algorithm at 715 cm^{-1}. CO2 Slicing had nearly 175% ($7.5 * 10^4$) more FOVs at 0 in the O-A plot than the NCEP Algorithm.

Of note, CO2 Slicing demonstrated the most compelling and convincing case for improving
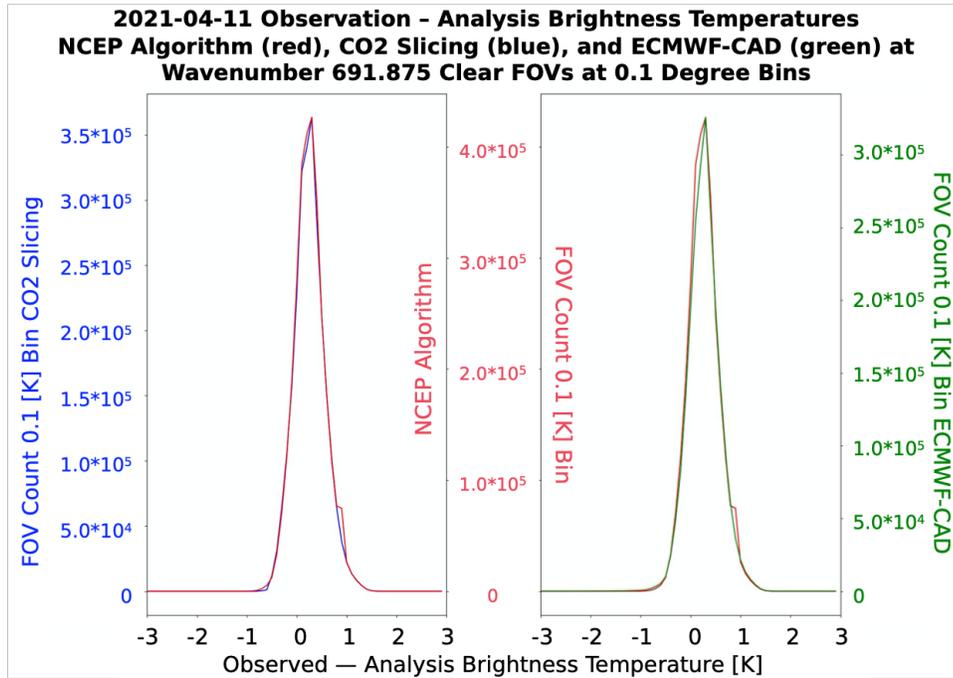
FIGURE 3.12: For the complex case test. O-A distribution plots are plotted using the central CO2 Slicing wavenumber 691.875 cm^{-1}. The NCEP Algorithm (red) was compared to ECMWF-CAD (green) and CO2 Slicing (blue). They are shown side by side for additional CO2 Slicing and ECMWF-CAD comparison. This is for all FOVs in the 24-hour period. For CO2 Slicing $\nu_1 = 691.875$ cm^{-1}.

the NCEP Algorithm using wavenumbers at and surrounding 715 cm^{-1} and for the upper troposphere. CO2 Slicing and the NCEP Algorithm performed with similar high accuracy at 691.875 cm^{-1} and 705 cm^{-1}. Despite the NCEP Algorithm having a higher quantity of FOVs at the peak than CO2 Slicing, 114.3% ($5 * 10^4$) and 140% (10^5) more FOVs respectively, these percent margins are still lower than at 715 cm^{-1}. Additionally, the lower number of clear CO2 Slicing FOVs at 691.875 cm^{-1} may be due to optically thin cirrus detection or incorrect classification on the part of the NCEP Algorithm. The miss classification of FOVs by the NCEP Algorithm is highlighted by using a confusion matrix of O-A plots at 691.875 cm^{-1} (Figure 3.19). In reviewing FOVs that the NCEP
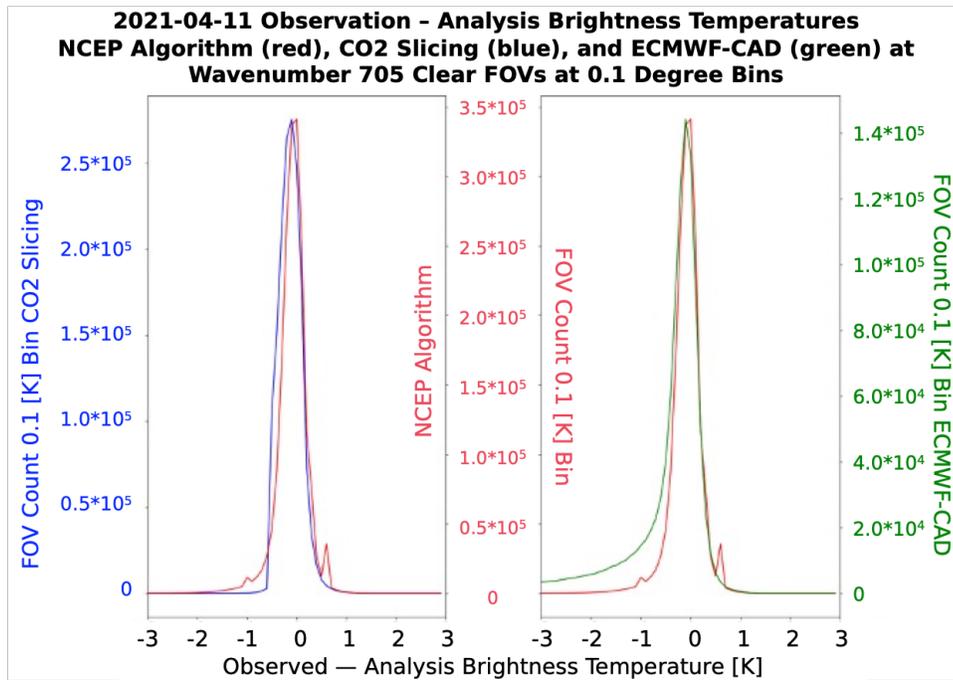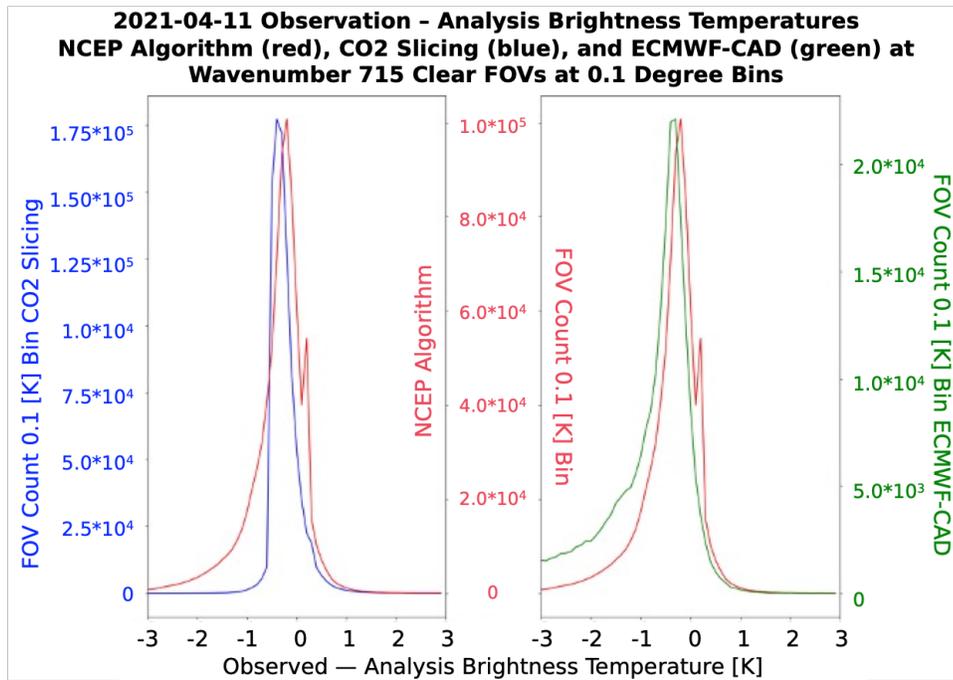
FIGURE 3.13: As with Figure 3.12, this is the O-A plots for 705 cm^{-1}. The NCEP Algorithm (red) was compared to ECMWF-CAD (green) and CO2 Slicing (blue). For CO2 Slicing ν_1 or $\nu_2 = 705$ cm^{-1}.

Algorithm as classified clear but CO2 Slicing classified as cloudy, there is evidence CO2 Slicing may have been correct. The distribution is multi peaked, and is not nearly as symmetric as the O-A plot for FOVs where both CO2 Slicing and the NCEP Algorithm agreed on a classification of clear. Also, the distribution of FOVs marked clear by CO2 Slicing but cloudy by the NCEP Algorithm demonstrates a loss of clear data assimilated. The distribution, which is nearly identical to the agreed clear FOV distribution, includes over $6 * 10^4$ FOVs with high likelihood of being clear.

At 715 cm^{-1} (Figure 3.21), the disparity between the classifications becomes even more evident. CO2 Slicing retains a symmetric distribution of clear classified FOVs for both for FOVs that agrees and FOVs that disagrees with the NCEP Algorithm. However, where
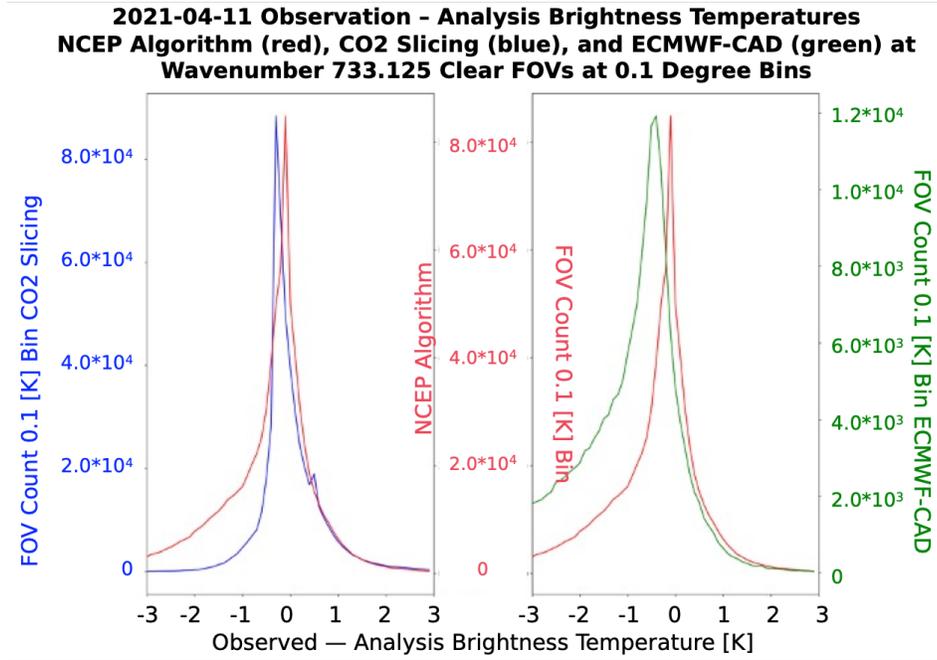
FIGURE 3.14: As with Figure 3.12, this is the O-A plots for 715 cm^{-1}. The NCEP Algorithm (red) was compared to ECMWF-CAD (green) and CO2 Slicing (blue). For CO2 Slicing ν_1 or $\nu_2 = 715$ cm^{-1}.

CO2 Slicing classified the FOV as cloudy and the NCEP Algorithm classified it as clear, the distribution is not symmetric. It has three district peaks at different O-A values, with one centered on 0 and two centered on negative values, and a slight cold tail. Moreover, the spatial distribution of clear CO2 Slicing but cloudy NCEP Algorithm FOVs were at polar latitudes and over land. The FOVs where they agreed occurred globally. But for the FOVs classified cloudy by CO2 Slicing but clear analyses by the NCEP Algorithm, where a substantial proportion could be wrongly classified clear by the NCEP Algorithm, are over the ocean. This leads credence to CO2 Slicing improving cloud classification on a global scale.

There were mixed results at 748.125 cm^{-1} and 959.375 cm^{-1} between CO2 Slicing and

FIGURE 3.15: As with Figure 3.12, this is the O-A plots for 733.125 cm^{-1}. The NCEP Algorithm (red) was compared to ECMWF-CAD (green) and CO2 Slicing (blue). For CO2 Slicing ν_1 *or* $\nu_2 = 733.125$ cm^{-1}.

the NCEP Algorithm. For instance, there was a significant cold tail on the 748.125 cm^{-1} (Figure 3.16) O-A plot for the NCEP Algorithm. While there is a slight double peak within CO2 Slicing curve, this could possibly be an artifact of the peaks being separated by one bin. Therefore, CO2 Slicing demonstrated an improvement to the NCEP Algorithm at the lower-mid atmosphere. Another example is the count of FOVs at O-A plot peak for 959.375 cm^{-1} (Figure 3.17). This is effectively the surface channel and can detect clear sky for the full atmosphere. In other words, a clear FOV at 959.375 cm^{-1} can be classified as clear for all other wavenumbers; the FOV is classified as cloud free for the whole atmospheric column. There were $2*10^4$ more cloud free FOVs with CO2 Slicing than with the NCEP Algorithm. However, 17.3% of NCEP Algorithm FOVs were
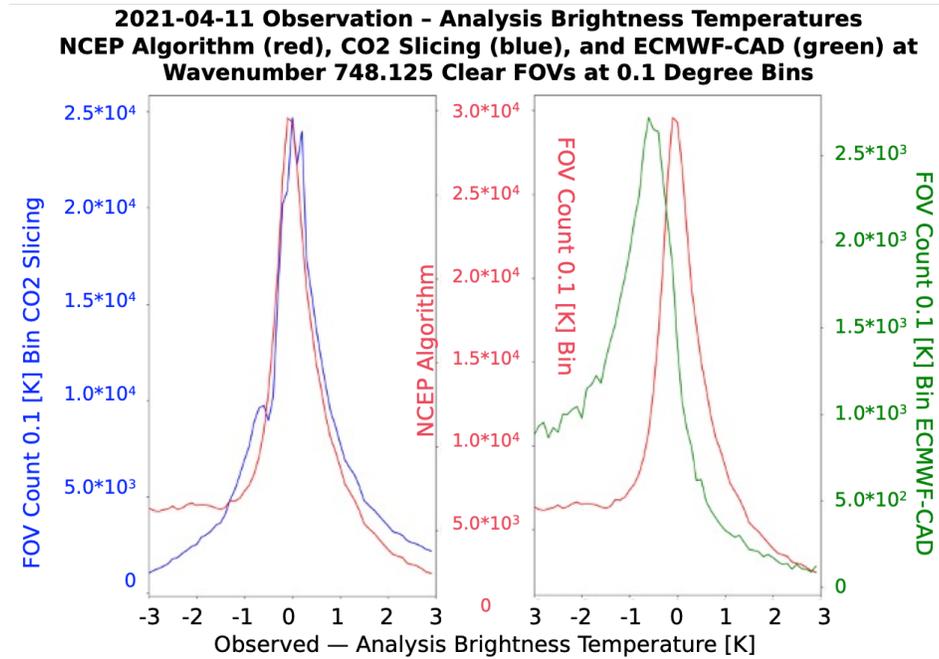
FIGURE 3.16: As with Figure 3.12, this is the O-A plots for 748.125 cm^{-1}. Thr NCEP Algorithm (red) was compared to ECMWF-CAD (green) and CO2 Slicing (blue). For CO2 Slicing $\nu_2 = 748.125$ cm^{-1}.

classified clear and 10.9% by CO2 Slicing (Figure 3.22). Plausibly the NCEP Algorithm both misclassified cloudy FOVs as clear and omitted include several clear FOVs.

In comparison to the simple case, the complex April test day was overall very similar. For the most part, the simple case results represent the complex case results very well. However, there were a few important differences that must be mentioned. At the lowest wavenumbers 691.875 cm^{-1}, the plots were nearly identical aside from the count of FOVs represented in the complex case versus the simple case. While the shapes of the 705 cm^{-1} curves were similar, with the simple case the clear FOV count for the NCEP Algorithm and CO2 Slicing are about the same. The complex case showed nearly a 10^5 FOV disparity with CO2 Slicing. This could have been caused by CO2 Slicing detecting more clouds over
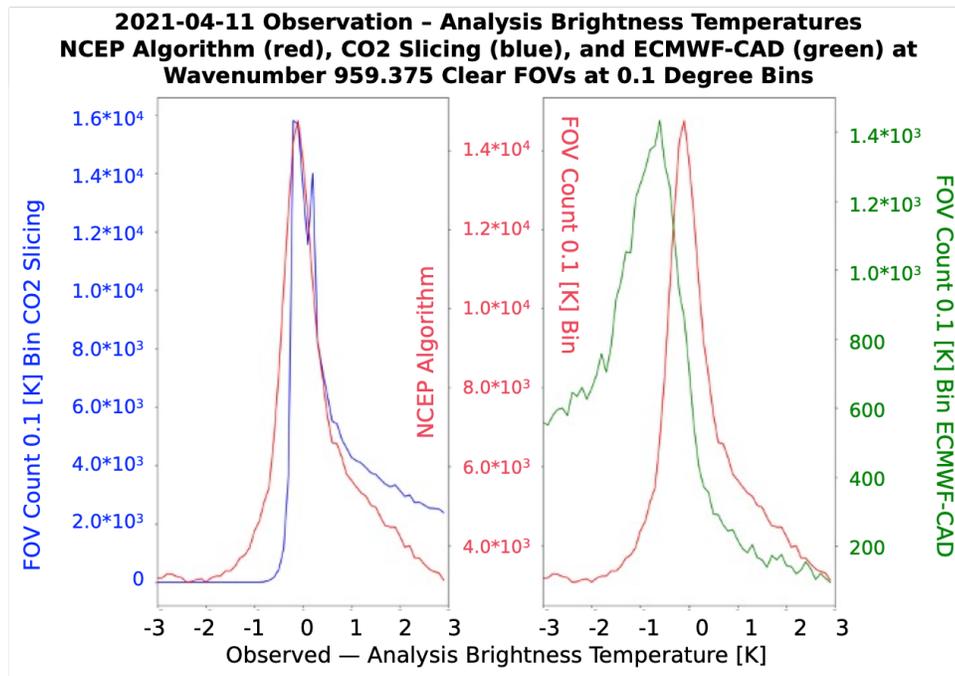
FIGURE 3.17: As with Figure 3.12, this is the O-A plots for the IR window wavenumber of 959.375 cm^{-1}. The NCEP Algorithm (red) was compared to ECMWF-CAD (green) and CO2 Slicing (blue).
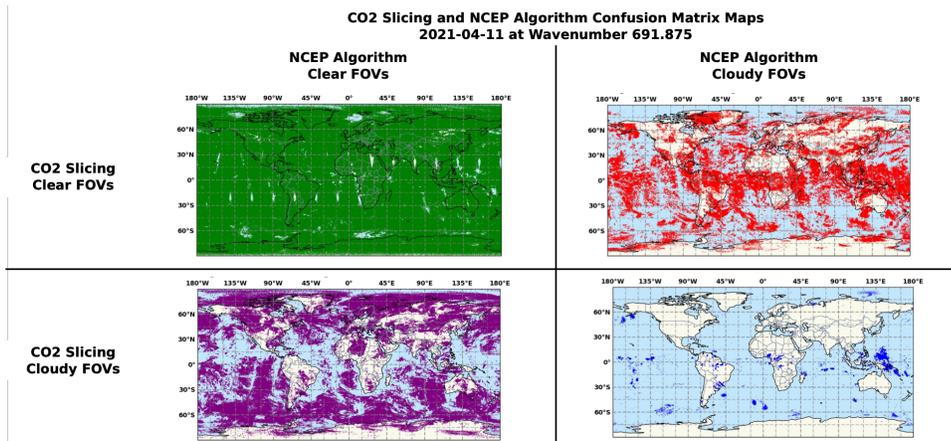

FIGURE 3.18: This confusion matrix for CO2 Slicing and the NCEP Algorithm is for 691.875 cm^{-1}. The two algorithms agreed classifying 72% of FOVs clear (top-left green) and 0.5% of FOVs cloudy (bottom-right blue). 10% of the FOVs were classified cloudy by the NCEP Algorithm but clear by CO2 Slicing (top-right red). 17.5% of the FOVs were classified clear by the NCEP Algorithm but cloudy by CO2 Slicing (bottom-left purple).
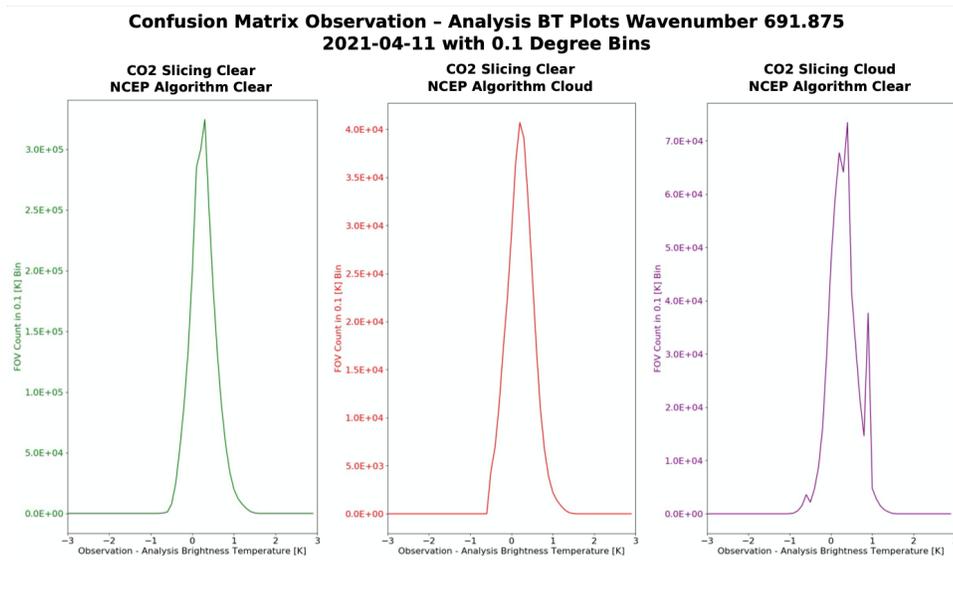
FIGURE 3.19: These O-A plots come from FOVs in the confusion matrix categories at 691.875 cm^{-1}. The left (green) plot comes from FOVs that both CO2 Slicing and the NCEP Algorithm identified clear. The center (red) plot is where CO2 Slicing marked the FOV clear, but the NCEP Algorithm marked it cloudy. The right (purple) plot is where CO2 Slicing marked the FOV cloudy, but NCEP marked it clear. FOVs classified cloudy by both algorithms were not plotted.
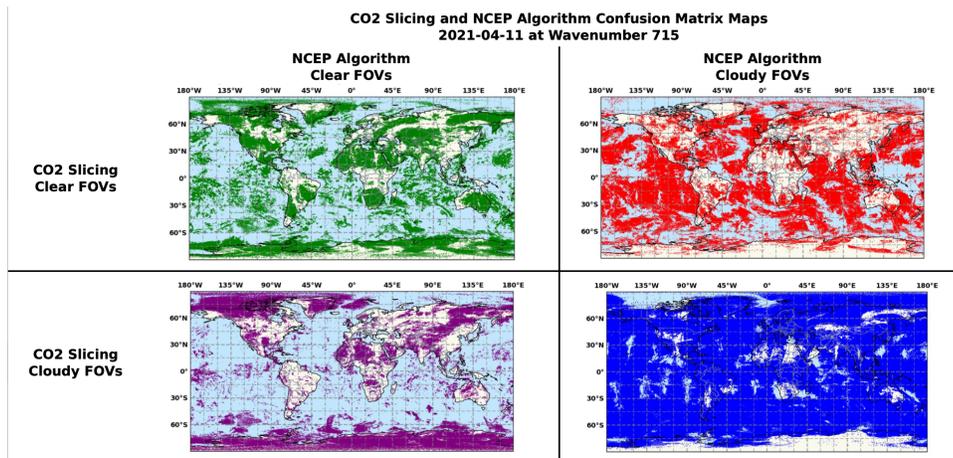

FIGURE 3.20: This confusion matrix for CO2 Slicing and the NCEP Algorithm is for 715 cm^{-1}. The two algorithms agreed classifying 13.8% of FOVs clear (top-left green) and 60.6% of FOVs cloudy (bottom-right blue). 15.3% of the FOVs were classified cloudy by the NCEP Algorithm but clear by CO2 Slicing (top-right red). 10.3% of the FOVs were classified clear by the NCEP Algorithm but cloudy by CO2 Slicing (bottom-left purple).
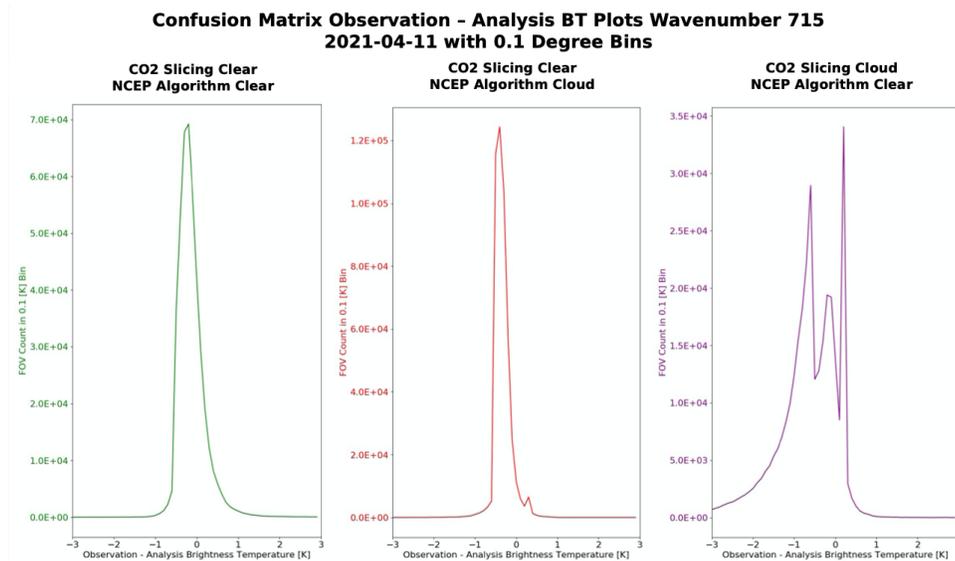
FIGURE 3.21: These O-A plots come from FOVs in the confusion matrix categories at wavenumber 715. The left (green) plot comes from FOVs that both CO2 Slicing and the NCEP Algorithm identified clear. The center (red) plot is where CO2 Slicing marked the FOV clear, but the NCEP Algorithm marked it cloudy. The right (purple) plot is where CO2 Slicing marked the FOV cloudy, but NCEP marked it clear. FOVs classified cloudy by both algorithms were not plotted.
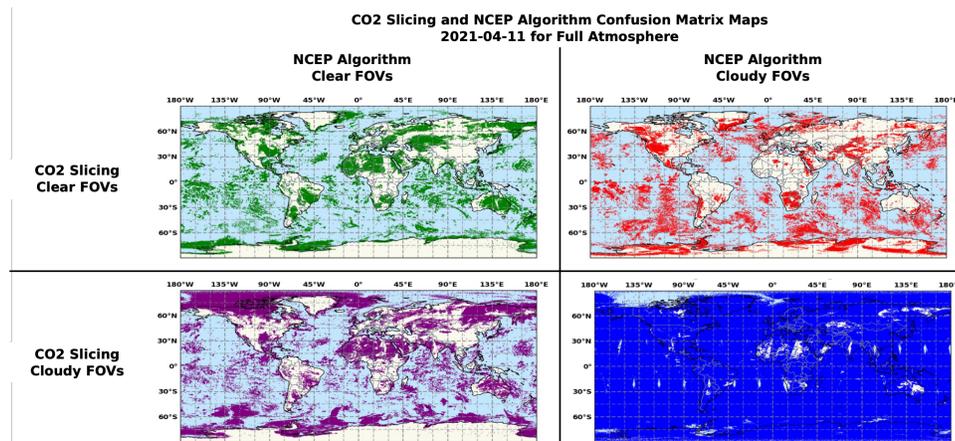

FIGURE 3.22: This confusion matrix for CO2 Slicing and the NCEP Algorithm for the full atmosphere. The two algorithms agreed classifying 6.7% of FOVs clear (top-left green) and 78.5% of FOVs cloudy (bottom-right blue). 4.2% of the FOVs were classified cloudy by the NCEP Algorithm but clear by CO2 Slicing (top-right red). 10.6% of the FOVs were classified clear by the NCEP Algorithm but cloudy by CO2 Slicing (bottom-left purple).

land and at polar regions. Plots for 715 cm^{-1} were also similar. The misclassifications with the NCEP Algorithm were more pronounced in the simple case than in the complex case, but the relative count of FOVs was comparable in the simple case and the complex case. Unlike at 705 cm^{-1}, at 733.125 cm^{-1} the shape of the O-A plots were similar but the CO2 Slicing and the NCEP Algorithm counts differ in the simple case. For the simple case, there was nearly 10^4 more FOVs classified clear with CO2 Slicing than with the NCEP Algorithm. This was perhaps due to enhanced cloud detection by the NCEP Algorithm over the Southern Hemisphere ocean (see Figure 3.22), compared to CO2 Slicing over land and poles. At 748.125 cm^{-1}, the CO2 Slicing curve's slight double peak and extra cold peak was more pronounced in the simple case than the complex case. Therefore, this feature must be a product of simple case conditions. Lastly at 959.375 cm^{-1}, the simple case peak count for CO2 Slicing was similar to the NCEP Algorithm. However, in the complex case, CO2 Slicing detected 2000 more clear FOVs than the NCEP Algorithm. This could mean that CO2 Slicing could enhance the NCEP Algorithm for land and polar clear sky detection. Moreover, there was a significant warm tail for the CO2 Slicing complex case, indicating there may be more impact from model error than CO2 Slicing algorithm error. Also note, there was only a 16.7% (200) FOV increase from the simple case to the complex case. This further confirms that ECMWF-CAD may not have been as effective as CO2 Slicing or the NCEP Algorithm.

3.3.3 Reproducibility and Validation

CO2 Slicing, by the simple and complex case results, was identified as the algorithm most plausible at improving the NCEP Algorithm. Consequently, this section will focus on just comparing CO2 Slicing to the NCEP Algorithm and VIIRS. O-A plots were primarily used in comparing the two algorithms on the three additional test days. But the visual confirmation method was used as an initial test.

From a preliminary inspection, CO2 Slicing and the NCEP Algorithm appear similar in cloud distribution globally like the April 2021 complex case (refer to Figure 3.23). There are, though, a few regions that highlight some features CO2 Slicing demonstrated in the April 2021 complex case. For the January 2021 case, a color corrected version of VIIRS indicates there were limited clouds over East Antarctica. While the NCEP Algorithm detected lower-level clouds for the entire land mass, CO2 Slicing correctly identified clear skies. Also on the January 2021 day, around 105E to 120E and 60N to 45N, the same color corrected VIIRS detected mostly cloudy FOVs. The NCEP Algorithm classified the majority of the region as clear, yet CO2 Slicing correctly classified many of the FOVs cloudy. On the July 2021 day, there are some fairly optically thin clouds over the western Sahara Desert, as visible with VIIRS. CO2 Slicing classified them as high clouds, whereas the NCEP Algorithm placed them much lower. At the gridded region 0 to 15W and 0 to 15S for the October 2020 day, the clouds are broken with several clear FOVs patches throughout. The NCEP Algorithm marked the entire region cloudy, but CO2 Slicing correctly identified several clear FOVs. Therefore, CO2 Slicing could have assisted the
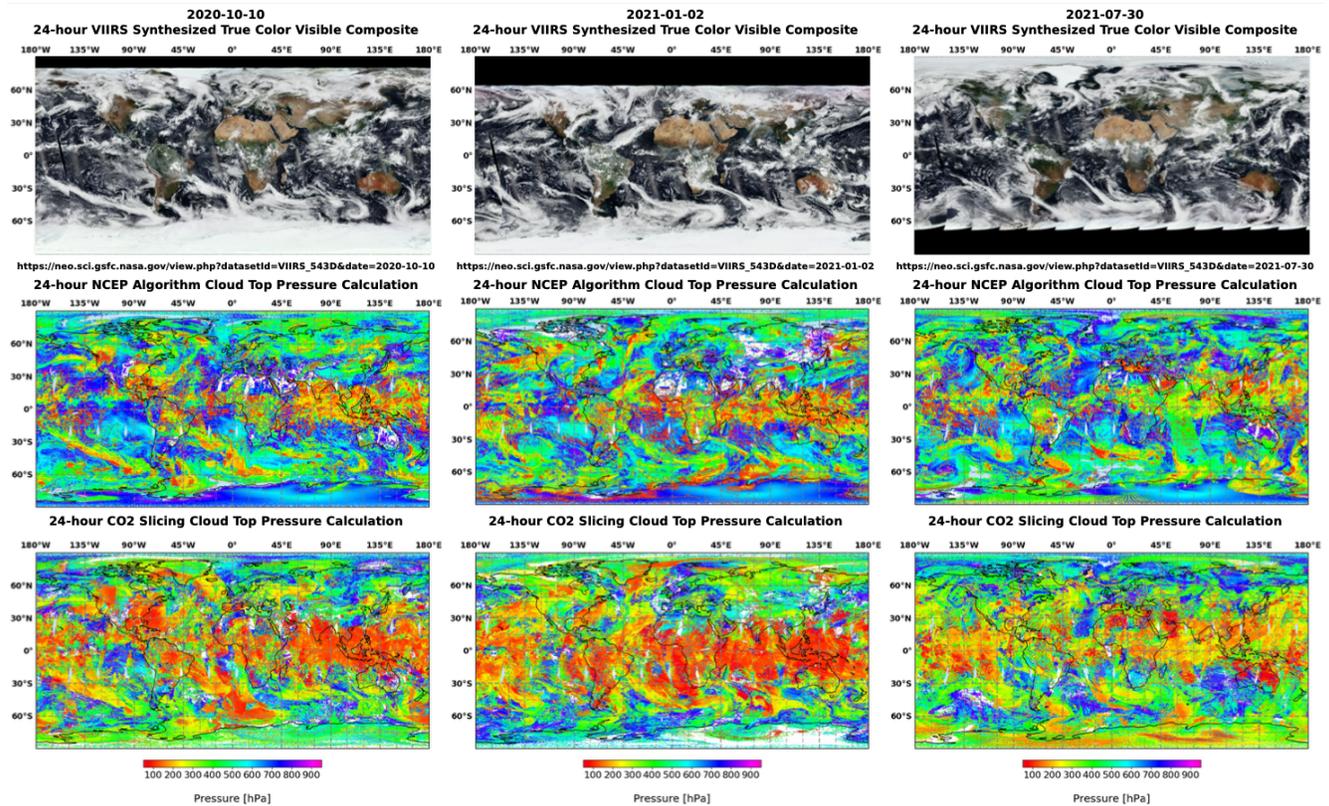
FIGURE 3.23: The top plots come from 24-hour VIIRS synthesized true color visible data composite archives. The middle plots come from the 24-hour calculated the NCEP Algorithm CTP. The bottom plots are the CO2 Slicing calculated CTP. Both the NCEP Algorithm and CO2 Slicing shared the same pressure color bar below. The three plots are from October 10, 2020 (left), January 2, 2021 (center), and July 20, 2021 (right).

NCEP Algorithm by eliminating cloudy FOVs higher up in the atmosphere for the July 2021 day, enhanced the number of clear FOVs on the January 2021 and October 2020 days, and eliminated cloud infected FOVs on the January 2021 day.

CO2 Slicing had similar O-A plot distributions for all of these days. For example, Figure 3.24 displays the CO2 Slicing O-A plot for 715 cm^{-1} for all test days on the same plot. The shape of the O-A plot curve was just as accurate and symmetric for the April 2021 day as it was for the October 2020, January 2021, and July 2021 days. The number

of FOVs at peak were relatively similar in value as well. These values were also consistently higher than the NCEP Algorithm peaks values. Overall, the O-A plots were similar throughout the 4 test days.

Moreover, the similarities between the cases is evident in the confusion plots. This was exemplified by looking at the FOVs where the two algorithms disagreed in classification. For example, at 715 cm^{-1} the O-A plots results were consistent over the 4 days. The distribution of FOVs classified clear from CO2 Slicing and cloudy from the NCEP Algorithm was very symmetric, has a very low range, and a relatively high peak across the test days (Figure 3.25). The distribution for FOVs classified cloudy from CO2 Slicing but clear from NCEP Algorithm had the same features throughout the test days (Figure 3.26). That is, the double peak was present on each of the distributions, as well as the cold tail. Therefore, it can be inferred that CO2 Slicing could have limited the number of data points that were incorrectly classified by the NCEP Algorithm, and included more clear FOVs into the assimilation.

3.4   Runtime

In addition to the improvement possible, the runtime of the algorithm was an important factor of comparison. For reference, the number of seconds and minutes matters as it pertains to algorithm runtime. With that said, it was critical that the algorithms require a similar amount of time as the NCEP Algorithm. As CO2 Slicing made the most
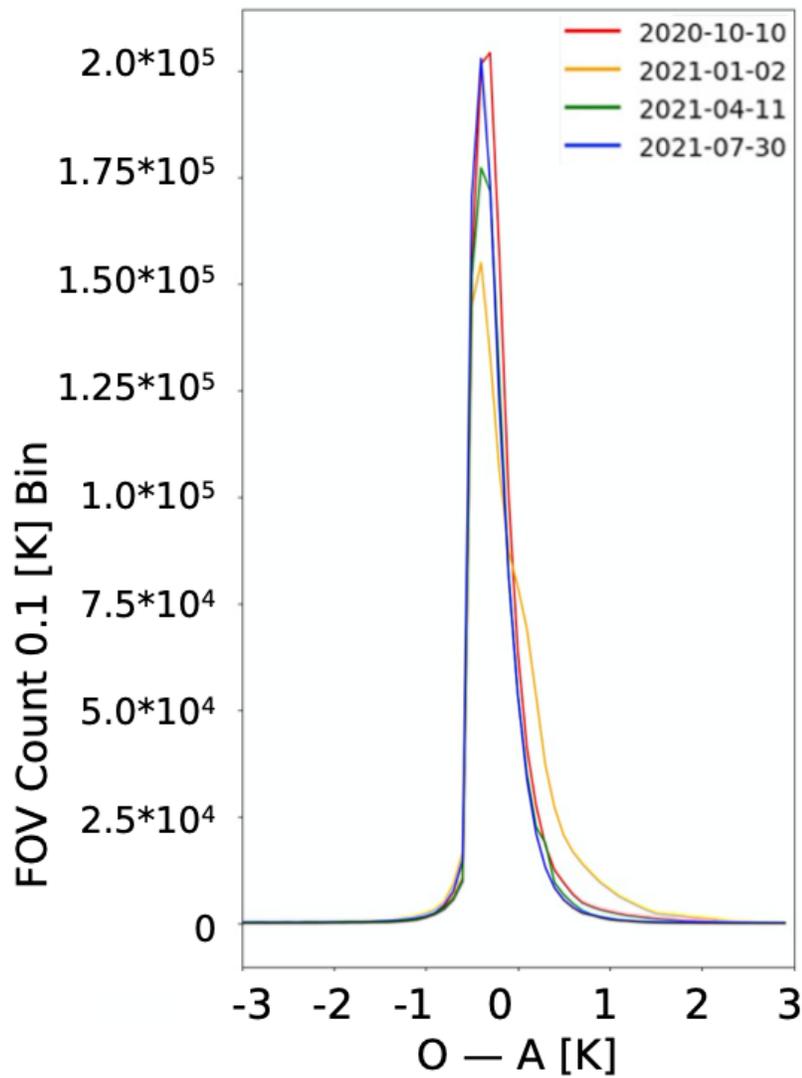
FIGURE 3.24: To demonstrate the similarity of CO2 Slicing result reproducibility, an O-A distribution plot was made at 715 cm^{-1} for each test day. They have then been plotted on the same plot, using the same y-axis.
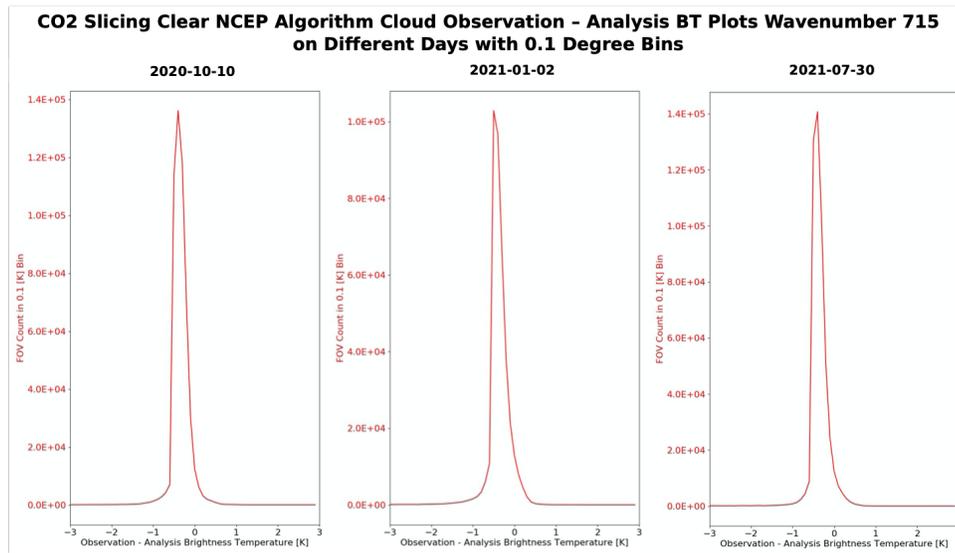
FIGURE 3.25: These are the O-A plots of FOVs classified as clear by CO2 Slicing but cloudy by NCEP Algorithm on the three other test days. All are at 715 wavenumbers. Left is the October 2020 day, center January 2021, and right July 2021.
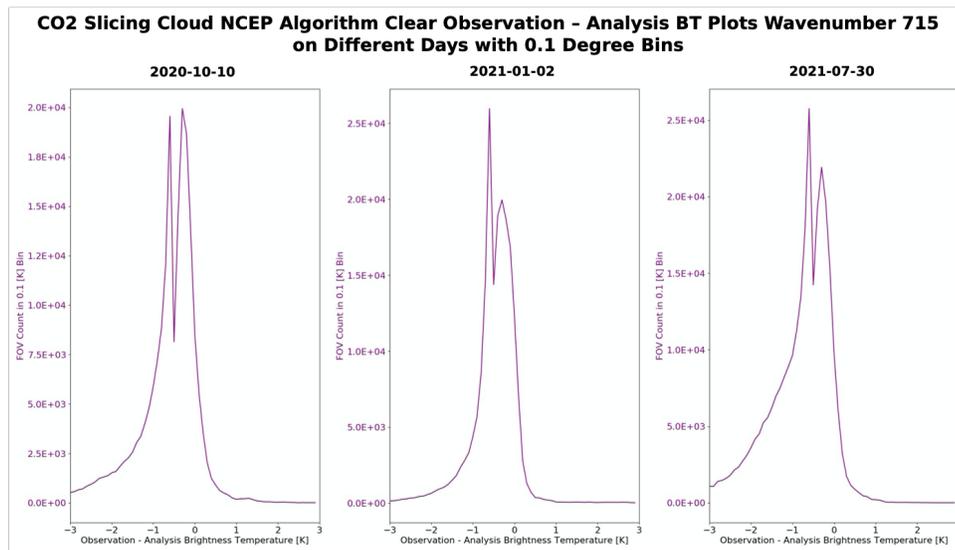

FIGURE 3.26: These are the O-A plots of FOVs classified as cloudy by CO2 Slicing but clear by NCEP Algorithm on the three other test days. All are at 715 wavenumbers. Left is the October 2020 day, center January 2021, and right July 2021.

convincing case of improving the NCEP Algorithm, only that algorithm will be tested against the NCEP Algorithm for runtime.

However, both algorithms were run using different coding languages. The NCEP Algorithm was written in FORTRAN and run as a Bash Shell script, and is operationally written and used as a FORTRAN subroutine within the GSI. The objective of this project was not to make the other algorithms operational. Rather it was to provide suggestions for improving the NCEP Algorithm by testing these algorithms. CO_2 Slicing was written for this project in Python for simplicity purposes (though it can easily be translated in to FORTRAN). But this variance of language changes the relevance of runtime. Python, at least within the structure of the way CO_2 Slicing was coded, is typically a slower program than FORTRAN. Because of this, the NCEP Algorithm and CO_2 Slicing runtimes were drastically different. Without making CO_2 Slicing operational, there is no fair deterministic way to address if CO_2 Slicing would be too computational expensive for the benefits it provides. Thus, runtime was not a factor included in the decision-making process.

Discussion

4.1   The Case for CO2 Slicing

Many aspects of CO2 Slicing could enhance the performance of the NCEP Algorithm, at least as demonstrated within the scope of this project. The case for CO2 Slicing can be summed into the following three points. Firstly, CO2 Slicing demonstrated its capability to improve clear radiance scheme by detecting more clear FOVs than the NCEP Algorithm. This was especially true for 715 cm^{-1} in Figure 3.25, but was also evident at other wavenumbers, such as 691.875 cm^{-1} (Figure 3.19). This wavenumber was significant because it enhanced a technique for detecting optically thin upper-level cirrus. Secondly, CO2 Slicing demonstrated its capability for correctly identifying cloudy FOVs, especially for FOVs the NCEP Algorithm incorrectly marked clear. Again, exemplified in 715 cm^{-1} in Figure 3.26 but demonstrated at other wavenumbers. This was displayed via a significant cold O-A difference. But CO2 Slicing marked these FOVs cloudy, which would have eliminated several cloud contaminated FOVs from the assimilation process. Thirdly, CO2 Slicing could improve cloud detection for more than just tropical, ocean FOVs. While the results of the simple case demonstrated CO2 Slicing could improve the NCEP Algorithm considerably, the complex case emphasized the global capabilities of CO2 Slicing. This was best demonstrated in 3.3.1 for polar and land FOVs. Note that

as it stands, the NCEP Algorithm is only one of many subsequent stages for downline forecasting. However, any FOVs excluded or included incorrectly at the NCEP Algorithm stage results in loss of valuable data for downline processes. Any cloudy FOVs not rejected by the NCEP Algorithm require the additional, potentially unnecessary computation time and memory, and could affect the downstream product. But the improvements that CO_2 Slicing demonstrated, the NCEP Algorithm could be optimized to include more clear and less cloudy FOVs.

4.2   Sources of Error

Sources of errors could be categorized into four groups: interpolation, input, user, and random. Spatial interpolation errors could have been introduced while comparing the 4 algorithms. Reprojecting the DR data to work with the other algorithms may have resulted in estimation of location errors. This would have appeared in the visual map analysis section of the results. However, detection of the spatial difference would have required a higher map resolution. Temporal interpolation errors could have also affected the visual map analysis. Because the NCEP Algorithm, DR, and CO_2 Slicing were plotted over a 24-hour period, there could have been overlaps in data. This would have not appeared on the VIIRS images. The best mitigation would be to have a lower resolution of spatial data points or to separate time intervals. Yet, changing the time intervals for plotting CTP data from 24-hours to a lower timeframe (e.g., 6-hour) would have caused VIIRS data to be operable with CTP data. Interpolation used in the FV3GFS could have affected the analyses input data. This would have been detected by O-A plots as

a warm tail. Although, warm tails are not exclusively a product of interpolation errors. Warm tails could have been a result of other errors in the analyses input data. The FV3GFS has several sources of potential errors that could affect the CRTM output, and could change the results (Tong et al., 2020). There could have been errors with the CRTM that could result in a warm tail. The input data from CrIS could have likewise resulted in a cold tail. The average error of CrIS is less than a degree, but higher for polar regions (Iturbide, 2021). The dataset was also relatively small, which could have effected the results. An extension of input error could be user error that could have occurred in running the algorithm software or code. User error could have also occurred when plotting the results, or during the analysis process. While all possible procedures were implemented to avoid such error, this source of error was ultimately unavoidable. Lastly, random errors would have come in the form of noise, which is unavoidable; the Gaussian distribution in the O-A plots demonstrated the presence of the random noise. The symmetry of the random noise was important. While the symmetry of the plots would have been detectable via O-A plots, it would have had relatively low impact on results.

4.3   Future Improvements and Next Steps

The logical next step will be to test suggestions made in this paper in an operational capacity. Specifically, NCEP will run and statistically analyze an operational version of CO2 Slicing as it compared to the current NCEP Algorithm. Aside from translating the Python script into FORTRAN, there are a few adjustments that could be made to this

version of CO2 Slicing. This includes implementing more CO2 channels, adjusting the cutoff value for different wavenumber pairs, and enhancing detection over desert regions. Though, as it stands, the current CO2 Slicing holds promise for improving the NCEP Algorithm, at least within the scope of this project. However, the full results will require a larger dataset and operational assimilation to determine the impact of including aspects of CO2 Slicing in NCEP high resolution IR cloud detection.

Conclusion

5.1 Conclusion

The objective of this paper and its research was to find an alternative to the NCEP Algorithm which could reliably select more clear FOVs and better reject cloudy FOVs. After an initial investigation, CO_2 Slicing demonstrated the best potential for improving upon the current NCEP Algorithm. As evident from the O-A plots, CO_2 Slicing was able to consistently detect clear FOVs that were classified cloudy by the NCEP Algorithm at several wavenumbers. CO_2 Slicing also demonstrated a marked improvement to cloudy FOV detection, best illustrated by rejecting cloudy FOVs that the NCEP Algorithm classified clear. In addition to providing better FOV classification for ocean, daytime, tropics to mid-latitude regions, CO_2 Slicing also exhibited improvements for land and polar FOV classification. CO_2 Slicing could also improve upon FOV classification for optically thin cirrus. Lastly, CO_2 Slicing demonstrated few disadvantages over the NCEP Algorithm. Therefore, CO_2 Slicing could improve the current algorithm without taking away any of the NCEP Algorithm's quality performance and advantages.

Bibliography

AMS, 2012a: atmospheric boundary layer re:pbl.

URL https://glossary.ametsoc.org/w/index.php?title=Atmospheric_boundary_layer&oldid=1968

— 2012b: tropopause.

URL https://glossary.ametsoc.org/w/index.php?title=Tropopause&oldid=4350

EOS, 2022: Noaa view data imagery portal.

URL https://neo.gsfc.nasa.gov/dataset_index.php#atmosphere

Hu, S. and G. K. Vallis, 2019: Meridional structure and future changes of tropopause height and temperature. *Quarterly Journal of the Royal Meteorological Society*, **145**, 2698–2717, doi:https://doi.org/10.1002/qj.3587.

Iturbide, F., 2021: Star jpss cross-track infrared sounder (cris).

URL https://www.star.nesdis.noaa.gov/jpss/CrIS.php

JCSDA, 2021: Community radiative transfer model (crtm).

URL https://www.jcsda.org/jcsda-project-community-radiative-transfer-model

Li, Z.-L., H. Wu, N. Wang, S. QIU, J. Sobrino, Z. WAN, B. Tang, and G. Yan, 2013: Land surface emissivity retrieval from satellite data. *International Journal of Remote Sensing*, **34**, 3084–3127, doi:10.1080/01431161.2012.716540.

Lim, A., J. Jung, H.-L. Huang, S. Ackerman, and J. Otkin, 1989: Assimilation of clear sky atmospheric infrared sounder radiances in short-term regional forecasts using community models. *Journal of Applied Remote Sensing*, **8**, doi:10.1117/1.JRS.8.083655.

Lin, S.-J., W. Putman, and L. Harris, 2017: The gfdl finite-volume cubed-sphere dynamical core. *NWS/NCEP/EMC*.

McNally, T. and P. Watts, 2003: A cloud detection algorithm for high-spectral-resolution infrared sounders. *Quarterly Journal of the Royal Meteorological Society*, **129**, 3411–3423, doi:0.1256/qj.02.208.

Menzel, P., 2009: *Remote Sensing Applications with Meteorological Satellites*. University of Wisconsin-Madison, Madison, WI.

Menzel, P., R. Frey, H. Zhang, D. Wylie, C. Moeller, R. Holz, B. Maddux, B. Baum, K. Strabala, and L. Gumley, 2008: Modis global cloud-top pressure and amount estimation: Algorithm description and results. *Journal of Applied Meteorology and Climatology*, **47**, 1175–1198, doi:10.1175/2007JAMC1705.1.

NASA, 2021: Visible infrared imaging radiometer suite (viirs).
URL https://earthdata.nasa.gov/earth-observation-data/near-real-time/download-nrt-data/viirs-nrt

Sassen, K., Z. Wang, V. Khvorostyanov, G. Stephens, and A. Bennedetti, 2002: Cirrus cloud ice water content radar algorithm evaluation using an explicit cloud microphysical model. *Journal of Applied Meteorology - J APPL METEOROL*, **41**, 620–628,

doi:10.1175/1520-0450(2002)041¡0620:CCIWCR¿2.0.CO;2.

Smith, W. L. S., E. Weisz, S. Kireev, D. Zhou, L. Zhenglong, and E. Borbas, 2012: Dual-regression retrieval algorithm for real-time processing of satellite ultra-spectral radiances. *Journal of Applied Meteorology and Climatology*, **51**, 1455–1476, doi:10.1175/JAMC-D-11-0173.1.

Tong, M., Y. Zhu, L. Zhou, E. Liu, M. Chen, Q. Liu, and S.-J. Lin, 2020: Multiple hydrometeors all-sky microwave radiance assimilation in fv3gfs. *Monthly Weather Review*, **148**, 2971–2995, doi:10.1175/MWR-D-19-0231.1.

Wang, P., J. Li, Z. Li, A. H. N. Lim, J. Li, T. J. Schmit, and M. D. Goldberg, 2017: The impact of cross-track infrared sounder (cris) cloud-cleared radiances on hurricane joaquin (2015) and matthew (2016) forecasts. *Journal of Geophysical Research: Atmospheres*, **122**, 13,201–13,218, doi:https://doi.org/10.1002/2017JD027515.

Warren, S., C. Hahn, J. London, R. Chervin, and R. Jenne, 1986: Global distribution of total cloud cover and cloud type amounts over land. *University Corporation for Atmospheric Research*, **No. NCAR/TN-273+STR**, doi:10.5065/D6GH9FXB.

Weisz, E., 2020: Installation instructions for the community satellite processing package (cspp) university of wisconsin (uw)-madison hyperspectral retrieval (hsrtv) software for direct broadcast version 2.0.
URL https://bin.ssec.wisc.edu/pub/CSPP/hidden/CrIS/EDR/hsrtv/v2.0/CSPP_HSRTV_Installation_Guide_v2.0a.pdf

Wylie, D. and P. Menzel, 1989: Two years of cloud covers statistics using vas. *Journal of Climate*, **2**, 380–392.

Zhang, H. and W. P. Menzel, 2002: Improvement in thin cirrus retrievals using an emissivity-adjusted co_2 slicing algorithm. *Journal of Geophysical Research (Atmospheres)*, **107**, 4327, doi:10.1029/2001JD001037.